Implementation and assessment of a two-scale computational framework for softening materials

Oriol Lloberas Valls

April 2006

Preface

The objective of this report is to introduce, implement and assess a two-scale FE technique for the mechanical study of heterogeneous quasi-brittle materials. Although the field of multi-scale analysis of structures is being intensively studied nowadays, some important issues regarding its applicability, convenience and performance remain unclear for certain engineering cases.

In this study a two-scale method is assessed that can deal with situations in which the scales are not completely separated or decoupled [18]. The size of the heterogeneities at a meso scale[1] are relevant compared to the macro-scale dimensions and, for this reason, it would affect the structural macro response. Strain localisation can develop during mechanical loading generating a spatial variation of the mechanical fields which would again violate the separation of scales principle. These characteristics are always present when studying failure processes of quasi-brittle materials such as concrete which is widely used in civil engineering structures.

The report is outlined starting in chapter one with a general introduction to different multi-scale strategies. Chapter two describes in detail the formulation of the two-scale selected methodology and its implementation in a standard finite element package (FEAP). Chapter three concentrates on the performance of the methodology when different constitutive models are tested. Some comments on the validation of the framework are given in chapter four. A brief discussion about the advantages and limitations of the implementation is provided in chapter five.

This work would not have been possible without the help and cooperation of all the colleagues from the Computational Mechanics Group at the Faculty of Civil Engineering and Geosciences of Delft University of Technology. A special word of thanks goes to my supervisors Prof. Bert Sluys and Dr. Angelo Simone for their guidance and support.

This research is part of the *strategisch basisonderzoek (SBO)* project IWT 03175 *'Structural damage due to dynamic excitations: a multi-disciplinary approach'*. Financial support is gratefully acknowledged.

---

[1] In the case of concrete the meso-level size can be as large as 1cm while the macro level size is of the order of meters.

Contents

Preface **3**

1 Overview of multi-scale strategies **11**
- 1.1 Setting the scene 11
- 1.2 Classification of multi-scale methods 11
  - 1.2.1 Analytical multi-scale approaches 12
  - 1.2.2 Computational multi-scale approaches 15

2 Formulation and implementation of a two-scale strong coupling method **21**
- 2.1 Framework formulation 21
- 2.2 Implementation in a standard FE package 24
  - 2.2.1 Generalities 24
  - 2.2.2 Particular implementation issues 29

3 Performance examples **31**
- 3.1 Linear Analysis 31
  - 3.1.1 Bar under uniaxial loading 31
  - 3.1.2 Bending test 33
- 3.2 Non-linear examples 37
  - 3.2.1 Bar under uniaxial loading 37
- 3.3 Framework extension for the gradient enhanced damage model 42
  - 3.3.1 Performance of the framework for a simple localisation test 42
  - 3.3.2 Performance of the framework for more complex localisation tests . 46

4 Framework validation **49**
- 4.1 Effect of the mesh discretisation 49
- 4.2 Effect of the step size 49
- 4.3 Influence of the penalty method 50

5 Discussion and recommendations **55**

A Gradient enhanced damage model **57**
- A.1 Basics of continuum damage mechanics 57
- A.2 Gradient-enhanced damage formulation 58

B Representative volumes for elastic, hardening and softening materials 61
B.1 Modeling a three phase brittle material 61
B.2 RVE considerations and size dependency 62

List of Figures

1.1 RVE with particle inclusions. 13
1.2 1st order scheme. 16
1.3 2nd order scheme. 17
1.4 Macro and meso discretisations for a strong coupling multi-scale technique. 19
1.5 Micro-macro compatibility based on Lagrange multipliers. 19

2.1 Linear interpolation of the meso boundary displacement field. 22
2.2 Linear interpolation coefficients of the transformation matrix T^e. 23
2.3 Incremental iterative scheme of the two-sale framework. 24
2.4 Two-scale framework implemented scheme. Communication between master, macro and meso programs. 26

3.1 Bar under uniaxial loading. 31
3.2 Left: Homogeneous discretisation (694 dofs). Right: Discretisation with void inclusions (804 dofs). 32
3.3 Force vs displacement plot at the right boundary. 32
3.4 Horizontal displacement contours (mm) at the macro-level (left) and meso-level (right) for the first (top) and second (bottom) discretisation. 33
3.5 Macro mesh for the bending test. 34
3.6 Left: Homogeneous discretisation (696 dofs). Right: Discretisation with void inclusions (762 dofs). 35
3.7 Force vs displacement plot at the top right node. 35
3.8 Vertical displacement contours (mm) at the macro-level (left) and meso-level (right) for the homogeneous (top), porous (middle) and weak porous (bottom) discretisation. 36
3.9 Uniaxial test for the multi-scale non-linear analysis 37
3.10 Top: Homogeneous meso-structure discretisation (set A: around 134 dofs) . Bottom: Void meso-structure discretisation (set B: 252 dofs for void discretisation). 38
3.11 Force displacement plot at the right boundary 38
3.12 Mono-scale horizontal displacement contours (Left) and horizontal stress contours (Right) 39

3.13 Horizontal Displacement contours for the macro-level structure (top) and meo cells (middle) corresponding to discretisation set A. Horizontal stress contours for discretisation set A (bottom) 40
3.14 Horizontal Displacement contours for the macro-level structure (top) and meso cells (middle) corresponding to discretisation set B. Horizontal stress contours for discretisation det B (bottom) 41
3.15 Meso-discretisation with weak inclusions. 43
3.16 Boundary conditions imposed to the macro-element in the multi-scale analysis (left) and meso structure for the mono-scale analysis (right). 43
3.17 Mono-scale analysis. Top to bottom: Displacement contours (left) and displacement profiles at the upper boundary (right), local equivalent strain contours (left) and local equivalent strain profiles at the upper boundary (right). 44
3.18 Multi-scale analysis. Top to bottom: Displacement contours (left) and displacement profiles at the upper boundary (right), local equivalent strain contours (left) and local equivalent strain profiles at the upper boundary (right). 45
3.19 Force displacement graph for mono and multi-scale analysis. 45
3.20 Tensile test for the porous structure (left) and mono-scale analysis discretisation (right). 46
3.21 Multi-scale analysis discretisation. Macro-mesh (left) and corresponding meso-discretisations (right). 47
3.22 Left to right: contour plots for the mono-scale and multi-scale tests. Top to bottom: Equivalent strain and vertical displacement (mm) contour plots. 47
3.23 Force displacement plot for multi and mono-scale tests. 48

4.1 Discretisation sets A (around 134 dofs) (top) and A fine (around 300 dofs (Bottom). 50
4.2 Left: Force displacement plots (set A and A fine). Right: Relative error plots for set A and A fine. 51
4.3 Step size dependency. Top: Mono-scale analysis force displacement plots. Bottom: Multi-scale analysis force displacement plots (left) and relative error (right). 52
4.4 Uniaxial loading test. 52
4.5 Top: Mechanical responses for standard b.c. (Left) and Penalty approach (Right). Middle: Relative error values between the two responses (Left) and 10 step analysis for different penalty weights. Bottom: Relative error values between the two responses for the optimal penalty weight. 53
4.6 Step size dependency for optimal penalty weight. Left: Multi-scale analysis force displacement plots. Right: Relative error graphics. 54
4.7 Penalty weight dependency for coarse step size discretisations in multi-scale analysis. Left: Multi-scale analysis force displacement plots. Right: Relative error graphics. 54

B.1 Granular material with aggregates matrix and an interfacial transition zone (left). Equivalent strain contours for the tensile test (right). 61
B.2 Meso cell size effect in softening. 62

Chapter 1

Overview of multi-scale strategies

1.1 Setting the scene

Multi-scale and multi-physics research aim at obtaining a sound constitutive description of engineering materials that would review pre-existing phenomenological material models. The increasing potential of modern computational tools has allowed many modeling techniques to extend its capabilities and work at a higher detailed level. By means of these strategies one can simulate the generation and evolution of inelastic processes that are often conditioned by highly heterogeneous structures at a lower scale.

Failure is one of the most complex problems in engineering mechanics. There are models available in literature (see appendix A) for the simulation of softening materials. Nevertheless, the generation of damage violates the principle of separation of scales as soon as deformations start to localise. For this reason the coupling between the two scales remains an unresolved issue when they are simultaneously treated. The formulation of a robust and general multi-scale framework that can naturally deal with these kind of problems is a challenging part of this research area.

The following section gives a brief overview of the most well-known multi-scale strategies.

1.2 Classification of multi-scale methods

It is difficult to follow a general criterion to classify most of the multi-scale approaches. Differences appear when trying to classify them from an engineering or mathematical point of view. Nowadays nomenclature is often confusing and is not completely standardized. It is not the intention in this report to give a general classification of all different strategies but rather define a basic classification between large groups of approaches.

The main issue in multi-scale mechanics is to identify the relationships that link various scales and set a framework in which information is treated and exchanged between all levels in an efficient way. In some cases it is possible to derive a *closed-form expression.* This is when the contribution of lower levels can be formulated analytically at the macro-level. In some other cases the geometry and/or the constitutive relation is too complex for an analytical derivation and a lower level response can only be computed by means of numerical simulations. The first general classification separates the cases in which it is possible to derive a closed-form expression (*analytical multi-scale approaches*) from the ones that it is not (*computational multi-scale approaches*).

1.2.1 Analytical multi-scale approaches

Homogenisation techniques are certainly the most widely known analytical methods. They were first developed within the framework of elasticity. Important homogenisation techniques such as Voigt-Reuss-Hill bounds among others [20] were developed and most of them are again used in parts of computational multi-scale approaches. Homogenisation of elastic and inelastic solids have been extensively studied (see [22] and [2]) but they turn out to be cumbersome when more complex physics or geometrical non-linearities are considered.

At a meso-level a representative volume RVE (see appendix B) is considered with all heterogeneities of the material. Effective properties are extracted via analytical procedures. At a macro-level macroscopic constitutive constants are substituted by the effective properties calculated over the RVE.

Some important issues of the homogenisation theory will be treated in this section and used in different multi-scale techniques.

Scale separation

Homogenisation theories are founded on the assumption that both macro and meso-levels are treated as a continuum. The former level is considered homogeneous while the later is represented heterogeneous. Each meso-specimen represents a material point at the macro-level. Different authors (see [14]) make emphasis on the scale separation principle because it is determinant on the use of mathematical homogenisation in certain multi-scale strategies.

> *The microscopic length scale l_m is assumed to be much smaller than the characteristic length l_M over which the size of the macroscopic loading varies in space.*

$$l_m << l_M$$

Effective properties for multi-phase materials

In this section an example of two-phase isothermal composites is briefly discussed introducing some well known homogenisation schemes such as the Voigt and Reuss models. The formulation is applicable when all inclusions are of the same shape, aspect ratio, orientation and material properties. For a complete overview of the extension to inelastic multi-phase materials the reader is referred to the work of Nemat Nasser and Hori [20] and Doghri [22], [2] among others.

In isothermal elasticity the macro stress $\boldsymbol{\sigma}$ and strain $\boldsymbol{\epsilon}$ tensors are related via the macro stiffness tensor $\boldsymbol{C}$

$$\boldsymbol{\sigma} = \boldsymbol{C}\colon\boldsymbol{\epsilon}. \tag{1.1}$$

In this example a representative volume V is composed of a matrix phase V_0 in domain ω_0 and an inclusion phase V_1 in domain ω_1 with volume fractions $\mathrm{v}_0 = V_0/V$ and $\mathrm{v}_1 = V_1/V = 1 - \mathrm{v}_0$, respectively (Figure 1.1).

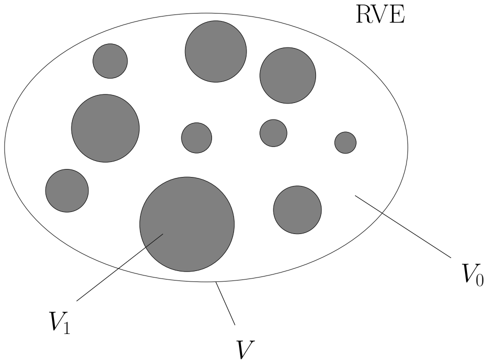

Figure 1.1: RVE with particle inclusions.

Averages of a field $\boldsymbol{f}$ over the entire RVE ω are denoted by

$$< \boldsymbol{f} >= \mathrm{v}_1 < \boldsymbol{f} >_{\omega_1} + (1 - \mathrm{v}_1) < \boldsymbol{f} >_{\omega_0}, \quad < \boldsymbol{f} >= \frac{1}{\mathrm{V}} \int_{\omega} \boldsymbol{f}\, \mathrm{dV} \tag{1.2}$$

The strain averages are related for each phase by a strain concentration tensor $\boldsymbol{B}$

$$< \boldsymbol{\epsilon}_{\omega_1} >= \boldsymbol{B}\colon < \boldsymbol{\epsilon}_{\omega_0} > . \tag{1.3}$$

For a general homogenisation model defined by $\boldsymbol{B}$ the homogenised macro-stiffness is given by

$$\bar{\boldsymbol{C}} = [v_1 \boldsymbol{C}_1\colon \boldsymbol{B} + (1 - v_1)\boldsymbol{C}_0]\colon [v_1 \boldsymbol{B} + (1 - v_1)\boldsymbol{I}]^{-1}, \tag{1.4}$$

being $\boldsymbol{I}$ the fourth-order symmetric identity tensor.

When assuming a uniform state of strain at the RVE $\boldsymbol{B} = \boldsymbol{I}$ (*Voigt model*) the following expression is found:

$$\bar{\boldsymbol{C}} = v_1 \boldsymbol{C}_1 + (1 - v_1)\boldsymbol{C}_0, \tag{1.5}$$

whereas the assumption of uniform stress $\boldsymbol{B} = \boldsymbol{C_1}^{-1}\colon \boldsymbol{C}_0$ (*Reuss model*) leads to

$$\bar{\boldsymbol{C}} = [v_1 \boldsymbol{C}_1^{-1} + (1 - v_1)\boldsymbol{C}_0^{-1}]^{-1}. \tag{1.6}$$

These well-known homogenisation schemes give upper and lower bounds for $\bar{\boldsymbol{C}}$, respectively. They are often used for simple cases to validate or compare the solution with more complex multi-scale strategies.

Averaging integrals

As introduced in (1.2) a certain quantity can be averaged over a domain by means of a volume integral. When the micro-structure is to be considered in more detail, average integrals of the strain and stress tensors can be computed as

$$\boldsymbol{\epsilon}_M = \frac{1}{V_m}\int_{V_m} \boldsymbol{\epsilon}_m \,\mathrm{dV_m} = ... = \frac{1}{A_m}\int_{A_m} \boldsymbol{x}_m\boldsymbol{n}_m \mathrm{dA_m}, \tag{1.7}$$

$$\boldsymbol{\sigma}_M = \frac{1}{V_m}\int_{V_m} \boldsymbol{\sigma}_m \,\mathrm{dV_m} = ... = \frac{1}{A_m}\int_{A_m} \boldsymbol{p}_m\boldsymbol{x}_m \mathrm{dA_m}, \tag{1.8}$$

where the Gauss-divergence theorem has been used. The subscripts M and m denote macro and micro-levels. V and A denote the volume and surface area of the representative volume. The tractions at the boundary are represented by $\boldsymbol{p}$. The position vector $\boldsymbol{x}$ at the boundary and its outward unit normal $\boldsymbol{n}$. It is shown that the averaged macroscopic stress tensor $\boldsymbol{\sigma}_M$ can be fully determined by the tractions $\boldsymbol{p}_m$ at the boundary of the representative volume.

An important integral average is the energy average theorem (*Hill-Mandel* condition). It states that the work variation average at the RVE is equal to the local work variation on the macro-scale.

$$\frac{1}{V_m}\int_{V_m} \boldsymbol{\sigma}_m\colon\delta\boldsymbol{\epsilon}_m \,\mathrm{dV_m} = \boldsymbol{\sigma}_M\colon\delta\boldsymbol{\epsilon}_M,\ \forall\delta\boldsymbol{x} \tag{1.9}$$

This condition is used in the sequel to verify energetical consistency of different boundary conditions for the micro to macro transitions.

RVE boundary conditions

Considering a RVE at a micro level, three different strategies are outlined to prescribe the boundary value problem departing from macro-scale quantities such as the deformation tensor. All three fullfill the Hill-Mandel condition and form a crucial part of the *macro* $\Longrightarrow$ *micro* $\Longrightarrow$ *macro* transition.

Fully prescribed displacements

The displacements at the prescribed boundary nodes are given by

$$\boldsymbol{u}_p = \boldsymbol{\epsilon}\cdot \boldsymbol{x}_p,\ \mathrm{p} = 1, 2, \ldots \mathrm{n}. \tag{1.10}$$

The approach has the same character of the Voigt method and leads to a slight overestimation of the RVE stiffness.

Uniform boundary tractions

The tractions at the boundary are prescribed in the following manner:

$$\boldsymbol{p}_p = \boldsymbol{P}\cdot \boldsymbol{n}_p,\ \mathrm{p} = 1, 2, \ldots \mathrm{n}, \tag{1.11}$$

being $\boldsymbol{P}$ the first Piola stress tensor, $\boldsymbol{n}_p$ the outward unit normal vector of the boundary nodes an $\boldsymbol{p}_p$ their corresponding prescribed tractions. The Hill-Mandel condition is violated when the same approach is formulated in terms of the Cauchy stress tensor $\boldsymbol{\sigma}$.

Periodic boundary conditions
Assuming a periodic distribution of the heterogeneous material the following approach can be formulated:

$$\boldsymbol{u}^{+} - \boldsymbol{u}^{-} = \boldsymbol{\epsilon} \cdot (\boldsymbol{x}^{+} - \boldsymbol{x}^{-}) \tag{1.12}$$

$$\boldsymbol{p}^{+} = -\boldsymbol{p}^{-}. \tag{1.13}$$

The superscripts $+$ and $-$ refer to the upper-right and lower-left boundary pairs of a quadrilateral specimen. Essential boundary conditions emerge from the assumption that opposite boundaries keep the same deformed geometry. Three corner nodes need to be prescribed and only one is set free. Tractions are opposite in opposite boundaries. This approach leads to results which are in between the bounds defined by the fully prescribed boundary tractions and fully prescribed boundary displacements. Although the averaged property will tend to be close to the fully prescribed displacement approach due to the fact that both are formulated in terms of essential boundary conditions.

1.2.2 Computational multi-scale approaches

These group of methods are characterized by the idea that the constitutive relation is extracted directly from micro-scale computations and inserted in the macro-scale via a hierarchical modeling framework (see reference [6]).

In this section two main groups of approaches are discussed. On one hand those techniques that make use of the previous homogenisation formulations (Section 1.2.1) and can be referred as *computational homogenisation* techniques [14] and the ones that are more linked to *substructuring*, *domain decomposition* and *scale coupling* methodologies [18].

Computational homogenisation multi-scale approaches

In the last years substantial work has been done regarding computational homogenisation of non-linear heterogeneous materials. Most of the techniques available in literature (see [26],[11],[19],[14]) are based on the solution of hierarchical or nested boundary value problems.

The main feature is that no constitutive relation is needed at the macro-level. All constitutive information comes naturally via the solution of boundary value problems at a micro-level (where the constitutive model is specified). One of the main advantages is that a complex micro-structure with different phases and non-linear mechanical behaviour can be modelled. The Finite Element Method [29] is one of the most common and suitable modeling strategies for the solution of boundary value problems.

The strategy is, although, computationally expensive however it can be used selectively, in some cases, over a specific domain.

According to Kouznetsova [7] two main strategies can be developed when considering first order or both first and second order gradients of the displacement field in the formulation. The strategies are briefly summarized in the following paragraphs.

First-order computational homogenisation

In this framework, a certain representative volume element RVE (see appendix B) is associated to a material point at the macro-level (i.e. a Gauss integration point in a FE setting). The principle of separation of scales described in Section 1.2.1 must be satisfied.

An exchange of data is performed between macro and meso levels as described in Figure 1.2 for a strain driven formulation. At each macro iteration a boundary value problem is built using the macro strain tensor $\boldsymbol{\epsilon}_M$ (see Section 1.2.1). Using a FE method, equilibrium is reached at the micro level. Stresses are averaged according to the homogenisation integrals summarized in Section 1.2.1 and the macro stress tensor $\boldsymbol{\sigma}_M$ is computed. A static condensation procedure [28] is applied to the stiffness matrix. First the system is partitioned into the coefficients corresponding to the prescribed p and free f degrees of freedom

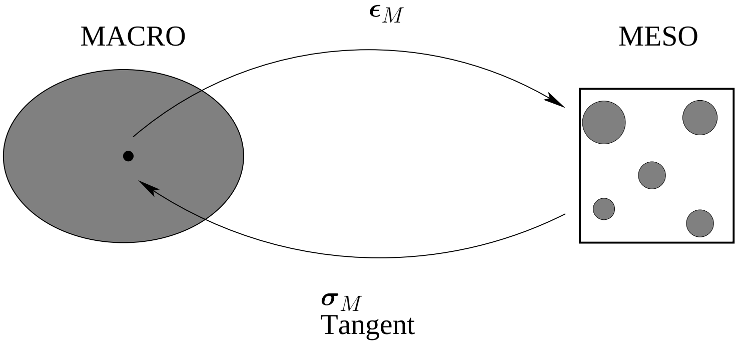

Figure 1.2: 1st order scheme.

$$\begin{bmatrix} \boldsymbol{K}_{pp} & \boldsymbol{K}_{pf} \\ \boldsymbol{K}_{fp} & \boldsymbol{K}_{ff} \end{bmatrix} \begin{bmatrix} \boldsymbol{u}_p \\ \boldsymbol{u}_f \end{bmatrix} = \begin{bmatrix} \boldsymbol{f}_p \\ \boldsymbol{f}_f \end{bmatrix}. \tag{1.14}$$

The condensed stiffness matrix is obtained for the case of prescribed boundary displacements

$$\boldsymbol{K}_c = \boldsymbol{K}_{pp} - \boldsymbol{K}_{pf}(\boldsymbol{K}_{ff})^{-1}\boldsymbol{K}_{fp}, \tag{1.15}$$

and the consistent tangent can be computed according to

$${}^4\boldsymbol{C}_M = \frac{1}{V}\sum_i \sum_j (\boldsymbol{X}_i \boldsymbol{K}_c \boldsymbol{X}_j)^{LC}, \tag{1.16}$$

where ${}^4\boldsymbol{C}_M$ is a fourth-order tensor, $\boldsymbol{X}$ the coordinates of the prescribed boundary nodes $i, j = 1..N_p$ and LC stands for left conjugation. The consistent tangent and the averaged stress tensor represent the constitutive relation adopted at the macro-level. Convergence is checked at the macro level and the incremental iterative procedure is continued.

The first order computational homogenisation approach is only applicable when scales remain separated. This is, when the micro-structure is very small compared to the macro-structure and no localisation can occur.

It can be proved that when combining this technique with a constitutive model at the lower scale that allows for softening and localisation, both macro element and micro-level size dependence are encountered [8]. The macro element size dependence can be explained by the assumed principle of local action [1]. All constitutive information is transfered from the meso level into a material point at the macro-level. Upon mesh refinement at the macro level the energy dissipated in the softening RVE is brought to a decreasing region (represented by the macro integration point). Hence, the problem at the macro level becomes ill-posed due to a lack of regularisation similarly to the effect observed in classical local constitutive softening models [1].

The meso size dependence is a purely phenomenological issue and is linked to the impossibility of finding a representative volume (as understood from classical homogenisation theories) for a softening material that experiences localisation [10] [17] [8] (See appendix B). Micro-level element size is solved since a higher order model is used for the constituents at micro-level.

Second-order computational homogenisation

In order to circumvent the previous drawbacks from the first-order scheme a second order framework is proposed and implemented by Kouznetsova et al. [15]. The main idea is to include higher order kinematics to the governing equations. The non-linear deformation map is now truncated to second order terms.

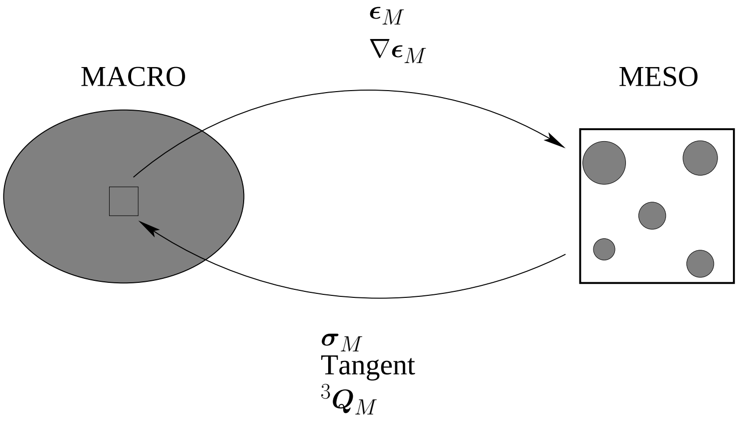

Figure 1.3: 2nd order scheme.

For this reason the deformation tensor $\boldsymbol{\epsilon}$ and the gradient $\nabla\boldsymbol{\epsilon}$ are needed to construct the boundary value problem at a micro level. Following a similar procedure as for the first order framework, the stress tensor $\boldsymbol{\sigma}$ and the third order stress tensor ${}^3\boldsymbol{Q}_M$ can be computed when equilibrium is reached at the micro level (Figure 1.3).

---

[1] The principle of local action states the relative independence of objects far apart in space (A and B): external influence on A has no direct influence on B.

The introduction of higher order kinematics allow for a non-local homogenisation scheme that automatically provides regularisation at the macro-level. This is, the framework does not suffer from macro-mesh dependence.

Although, as argued by Gitman in [8] the second order computational homogenisation scheme still presents meso/micro-size dependence.

Multi-scale methods with coupled scales

In this section a general overview is provided about those methods which consider that the meso and macro scales are fully coupled and, for this reason, the meso-scale specimens occupy a specific volume of the macro-structure. The macro structure can be divided in certain domains composed by one or more macro elements. Information is brought to the domain boundaries from the macroscopic solution in order to prescribe a certain boundary condition. The subdomains can be solved independently and the condensed element constitutive information is sent back to the macro-structure.

The idea is very much related to *substructuring* [23] or *domain decomposition* techniques [5] although a fundamental difference can be made. In multi-scale analysis the macro structure is first studied as an homogeneous structure without considering detailed information of heterogeneous subdomains. With the results of a global analysis the boundary conditions are imposed to the local detailed structure parts. Following a similar procedure as in computational homogenisation methods (Section 1.2.2) the analysis can be performed globally to all meso-cells or using selective criteria. This is, only in critical areas, a more detailed study is performed.

A key point for these kind of analyses are the boundary conditions applied to the lower scale boundaries. This is of crucial importance when adjacent boundaries from meso and macro levels do not match (in terms of number and position of nodes). In these cases care must be taken when imposing the boundary conditions. In a similar fashion as exposed in Subsection 1.2.1 the boundary conditions can be displacement (essential) or force (natural) based being an interpolation of these fields along the prescribed boundaries.

Coupled-volume approach

This technique is introduced by Gitman in [9], [8] and can be seen as an extension of the first-order computational homogenisation method (see Section 1.2.2). The main difference is that now the area occupied by the mesoscopic cell is linked (made equal) to the area corresponding to one macro integration point. In the case that only one integration point is used at the macro finite element the meso cell and macro element sizes are uniquely linked. The data exchange between macro and meso levels is equivalent to the first order scheme (namely the tensors $\boldsymbol{\sigma}$, $\boldsymbol{\epsilon}$ and the constitutive moduli $\boldsymbol{D}$). For that reason, the boundary conditions for the macro to meso transition need to be of the type exposed in Section 1.2.1. The nature of these boundary conditions is linked to a

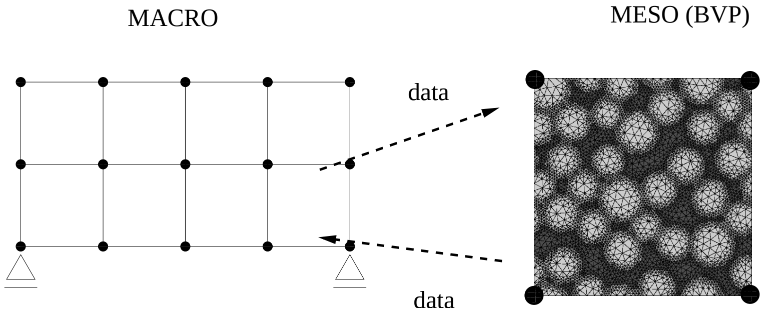

Figure 1.4: Macro and meso discretisations for a strong coupling multi-scale technique.

classical homogenisation scheme and, for this reason, they do not directly fit in a context in which the scales remain coupled.

Strong coupling multiscale techniques

The following method is proposed by Ibrahimbegović and Marcovič in [18]. It is classified as a multi-scale method that deals with coupled scales. Each macro element has a corresponding meso-cell which matches completely in terms of shape and dimensions as illustrated in Figure 1.4. For this reason the meso-macro interface is then easier to construct. The meso specimens can be discretised by different element types.

The scales are coupled via localised Lagrangian multipliers (Figure 1.5) which constitute an interface between meso and macro structures. They basically provide compatibility for meso and macro displacement fields. Both force and displacement interfaces can be developed within the framework of Lagrange multipliers.

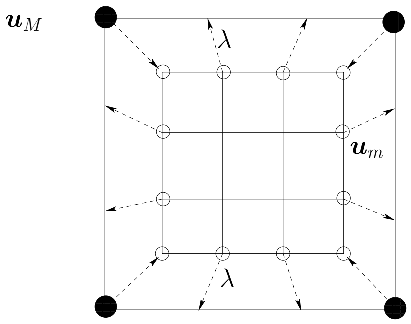

Figure 1.5: Micro-macro compatibility based on Lagrange multipliers.

A hierarchical strategy can be written in which macro level equilibrium, meso-macro compatibility and meso level equilibrium are fullfilled. An iterative Newton Raphson procedure can be chosen to reach convergence at any of the three main parts of the nested scheme in order to ensure the robustness of the method.

The method is valid in those cases in which the separation of scales principle does not hold and fits entirely in a hierarchical FE multi-scale framework. In the next chapter a detailed implementation of the described approach is given for a certain choice of the boundary interface. The performance of the framework is assessed for linear elasticity, standard plasticity and the gradient enhanced damage model (see appendix A).

Chapter 2

Formulation and implementation of a two-scale strong coupling method

In the following a two scale strong coupling method is formulated for the case of a *displacement interface*. In the same fashion as explained in Section 1.2.2 (strong coupling multi-scale techniques), every macro element has a corresponding meso-cell with identical shape and dimensions. Macro-elements are constituted by four-noded quadrilateral elements and meso-specimens are formed, at the same time, by an arbitrary FE type. The framework is formulated in an incremental iterative fashion so that it is valid for studying the response of a non-linear material. At the macro-level no constitutive law is specified whereas at the meso-level all phases of the heterogeneous material are identified by its inelastic law. The data exchange between macro and meso level is performed at the element level of the macro computations where element quantities are formed after the solution of the corresponding meso boundary value problems.

2.1 Framework formulation

At each macro iteration (i) the linearized system of equations

$$\boldsymbol{K}^i \, d\boldsymbol{u}^{M,i+1} = \boldsymbol{r}^i \tag{2.1}$$

needs to be solved, where $d\boldsymbol{u}^{M,i+1} = \boldsymbol{u}^{M,i+1} - \boldsymbol{u}^{M,i}$ is the iterative displacement vector and $\boldsymbol{r}^i = \boldsymbol{f}^{ext} - \boldsymbol{f}^{int,i}$ represents the residual at each iteration i. In the present framework the global stiffness matrix $\boldsymbol{K}^i$ and the right hand side $\boldsymbol{r}^i$ are determined by the assembly of the element stiffness matrices and RHS that emerge from the converged solution of meso scale boundary value problems. Each macro element is assigned a meso specimen for which a boundary value problem can be constructed based on the iterative displacements at the four corner nodes. This procedure can be written in a matrix notation (2.2) where the transformation matrix $\boldsymbol{T}^e$ sets the link between the displacements at the four corner nodes of the macro element and the displacements at the boundary of the corresponding meso specimen.

$$\bar{\boldsymbol{u}}^{m,e,i} = \boldsymbol{T}^{e}\boldsymbol{u}^{M,e,i}. \tag{2.2}$$

In this implementation $\boldsymbol{T}^e$ is chosen to be the linear interpolation between to adjacent macromesh nodes as depicted in Figure 2.1.

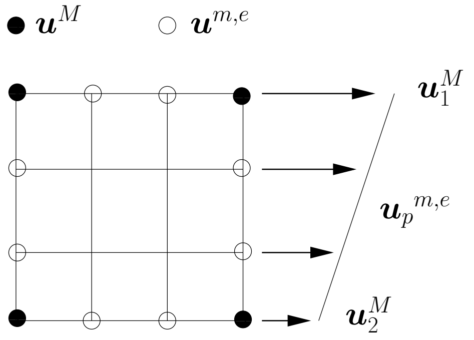

Figure 2.1: Linear interpolation of the meso boundary displacement field.

Equation (2.2) can be rewritten in a more detailed form according to the expression

$$\begin{bmatrix} \boldsymbol{u}_1^m \\ \vdots \\ \boldsymbol{u}_n^m \\ \boldsymbol{u}_{n+1}^m \\ \vdots \\ \boldsymbol{u}_{n+m-1}^m \\ \boldsymbol{u}_{n+m}^m \\ \vdots \\ \boldsymbol{u}_{n+m+t-2}^m \\ \boldsymbol{u}_{n+m+t-1}^m \\ \vdots \\ \boldsymbol{u}_{n+m+t+s-4}^m \end{bmatrix} \begin{bmatrix} \boldsymbol{a}_1 & \boldsymbol{b}_1 & 0 & 0 \\ \vdots & \vdots & \vdots & \vdots \\ \boldsymbol{a}_n & \boldsymbol{b}_n & 0 & 0 \\ 0 & \boldsymbol{c}_2 & \boldsymbol{d}_2 & 0 \\ \vdots & \vdots & \vdots & \vdots \\ 0 & \boldsymbol{c}_m & \boldsymbol{d}_m & 0 \\ 0 & 0 & \boldsymbol{e}_2 & \boldsymbol{f}_2 \\ \vdots & \vdots & \vdots & \vdots \\ 0 & 0 & \boldsymbol{e}_t & \boldsymbol{f}_t \\ \boldsymbol{h}_2 & 0 & 0 & \boldsymbol{g}_2 \\ \vdots & \vdots & \vdots & \vdots \\ \boldsymbol{h}_{s-1} & 0 & 0 & \boldsymbol{g}_{s-1} \end{bmatrix} = \begin{bmatrix} \boldsymbol{u}_1^M \\ \\ \boldsymbol{u}_2^M \\ \\ \boldsymbol{u}_3^M \\ \\ \boldsymbol{u}_4^M \end{bmatrix}, \tag{2.3}$$

with

$$\begin{aligned} \boldsymbol{a} &= 1 + \tfrac{\boldsymbol{X}-X_1}{X_1-X_2} & \boldsymbol{b} &= \tfrac{X_1-\boldsymbol{X}}{X_1-X_2} \\ \boldsymbol{c} &= 1 + \tfrac{\boldsymbol{X}-Y_2}{Y_2-Y_3} & \boldsymbol{d} &= \tfrac{Y_2-\boldsymbol{X}}{Y_2-Y_3} \\ \boldsymbol{e} &= 1 + \tfrac{\boldsymbol{X}-X_3}{X_3-X_4} & \boldsymbol{f} &= \tfrac{X_3-\boldsymbol{X}}{X_3-X_4} \\ \boldsymbol{g} &= 1 + \tfrac{\boldsymbol{X}-Y_4}{Y_4-Y_1} & \boldsymbol{h} &= \tfrac{Y_4-\boldsymbol{X}}{Y_4-Y_1}. \end{aligned} \tag{2.4}$$

The boldfaced coefficients denote vectors with x and y components. The subscripts 1 to 4 denote the four corner nodes of the macro element. The subscripts n, m, t and

s correspond to the number of boundary nodes at each quadrilateral side of the meso specimen. The arrays $\boldsymbol{a}$, $\boldsymbol{b}$, $\boldsymbol{c}$, $\boldsymbol{d}$, $\boldsymbol{e}$, $\boldsymbol{f}$, $\boldsymbol{g}$ and $\boldsymbol{h}$ contain the coefficients for the linear interpolation at each boundary side (Figure 2.2).

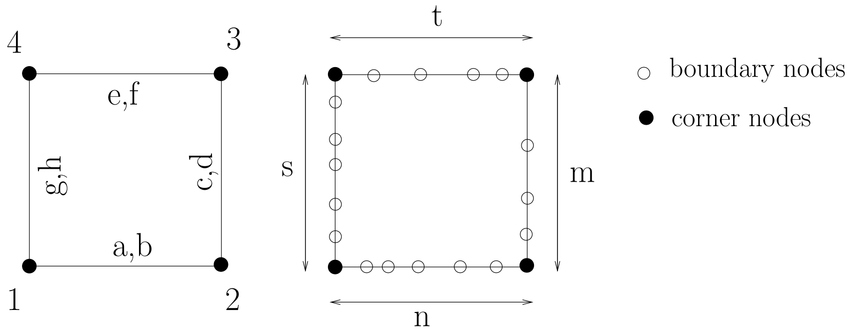

Figure 2.2: Linear interpolation coefficients of the transformation matrix T^e.

The coordinate vectors $\boldsymbol{X}$ contain the two components x and y of the two dimensional space and represent the position of each boundary nodal point which displacement vector is interpolated. The coordinates $X_1, \ldots, X_4$ and $Y_1, \ldots, Y_4$ correspond the position of the four corner nodes used for the interpolation to the rest of the boundary.

After constraining displacements at the boundary of the meso level a number of iterations is needed to solve the non-linear problem and reach equilibrium. It is assumed that all computations at the meso level depart from the last equilibrium stage reached in the previous step. This includes the update of all internal and state variables. The linearized problem to be solved at the meso level reads

$$\boldsymbol{K}^{m,e,j}\, d\boldsymbol{u}^{m,j+1} = \boldsymbol{r}^{m,j}, \tag{2.5}$$

where $d\boldsymbol{u}^{m,j+1} = \boldsymbol{u}^{m,j+1} - \boldsymbol{u}^{m,j}$ is the iterative displacement vector and $\boldsymbol{r}^{m,j} = \boldsymbol{f}^{m,ext,j+1} - \boldsymbol{f}^{m.int,j}$ represents the residual at each meso iteration j. In the same fashion as in (1.14) the system can be split into the free and constrained parts. When convergence is reached at the meso level the matrix representation of the system containing the prescribed and free parts reads

$$\begin{bmatrix} \boldsymbol{K}_{pp}^{m,e} & \boldsymbol{K}_{pf}^{m,e} \\ \boldsymbol{K}_{fp}^{m,e} & \boldsymbol{K}_{ff}^{m,e} \end{bmatrix} \begin{bmatrix} d\boldsymbol{u}_p^{m,e} \\ d\boldsymbol{u}_f^{m,e} \end{bmatrix} = \begin{bmatrix} \boldsymbol{r}_p^{m,e} \\ \boldsymbol{r}_f^{m,e} \to \boldsymbol{0} \end{bmatrix}. \tag{2.6}$$

The mechanical information contained in the system can be projected to the boundaries using the static condensation of Wilson [28]

$$\hat{\boldsymbol{K}}^{m,e} d\boldsymbol{u}_p^{m,e} = \hat{\boldsymbol{r}}^{m,e}, \tag{2.7}$$

where the condensed stiffness matrix and right hand side have the following expression

$$\hat{\boldsymbol{K}}^{m,e} = \boldsymbol{K}_{pp}^{m,e} - \boldsymbol{K}_{pf}^{m,e} (\boldsymbol{K}_{ff}^{m,e})^{-1} \boldsymbol{K}_{fp}^{m,e} \tag{2.8}$$

$$\hat{\boldsymbol{r}}^{m,e} = \boldsymbol{r}_p^{m,e} - \boldsymbol{K}_{pf}^{m,e} (\boldsymbol{K}_{ff}^{m,e})^{-1} \boldsymbol{r}_f^{m,e} = \boldsymbol{r}_p^{m,e}. \tag{2.9}$$

A last transformation is needed to convert the condensed information into the appropriate macro element quantities.

$$\boldsymbol{K}^{M,e,i} = \boldsymbol{T}^{e,T}\hat{\boldsymbol{K}}^{m,e}\boldsymbol{T}^{e} \tag{2.10}$$

$$\boldsymbol{r}^{M,e,i} = \boldsymbol{T}^{e,T}\hat{\boldsymbol{r}}^{m,e}. \tag{2.11}$$

Once all macro element stiffness and RHS are computed they are assembled into $\boldsymbol{K}^{i}$ and $\boldsymbol{r}^{i}$ and inserted in (2.1). The operation is repeated for each macro loading step until convergence is reached at the macro level (see Figure 2.3). Because an iterative Newton Raphson procedure is used both at macro and meso levels the convergence of the scheme is guaranteed.

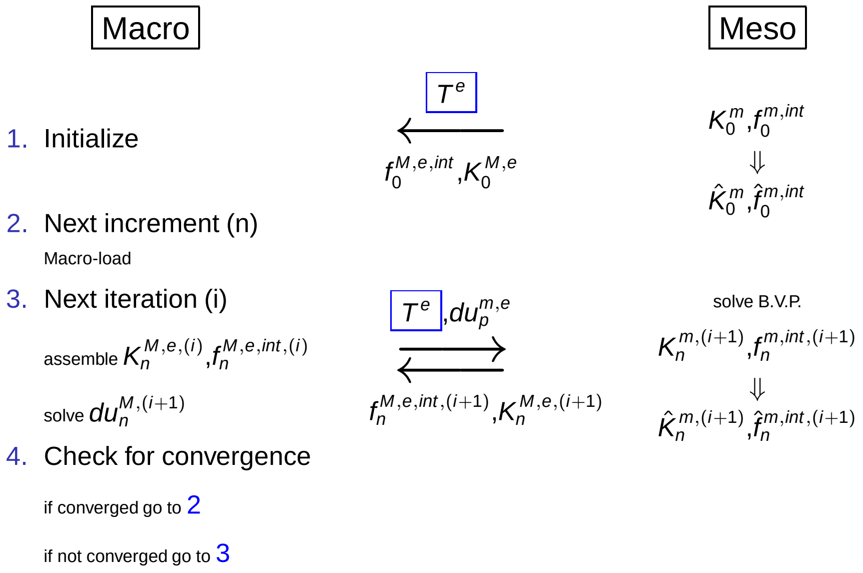
Macro
Meso
T^e
1. Initialize
$K_0^m, f_0^{m,int}$
$\Downarrow$
$\hat{K}_0^m, \hat{f}_0^{m,int}$
$f_0^{M,e,int}, K_0^{M,e}$
2. Next increment (n)
Macro-load
3. Next iteration (i)
T^e, $du_p^{m,e}$
solve B.V.P.
assemble $K_n^{M,e,(i)}, f_n^{M,e,int,(i)}$
$K_n^{m,(i+1)}, f_n^{m,int,(i+1)}$
$\Downarrow$
solve $du_n^{M,(i+1)}$
$f_n^{M,e,int,(i+1)}, K_n^{M,e,(i+1)}$
$\hat{K}_n^{m,(i+1)}, \hat{f}_n^{m,int,(i+1)}$
4. Check for convergence
if converged go to 2
if not converged go to 3

Figure 2.3: Incremental iterative scheme of the two-sale framework.

2.2 Implementation in a standard FE package

2.2.1 Generalities

The two scale framework is implemented in the FE package FEAP [27]. The program is used to perform both macro and meso FE computations.

Several modifications in the data input and solution module are established. The code interprets certain instructions written in the input file that indicate the program to perform either macro or meso level computations. An external file sets the links between macro-elements and its corresponding mesoscopic mesh. When selective multi-scale analysis is performed not all macro-elements are specified in this connectivity file.

Each meso mesh has a corresponding input file specifying all material data for the different phases. Different material models can be chosen for each phase and each mesoscopic specimen at the same time. No material model is active at the macro level except for the case of selective multi-scale analysis. In this situation a standard linear elastic model is used at the element level for non-critical areas.

Data exchange between macro and meso computations is stored in files. The exchange is performed at the element level of the macro computations. At this point two FEAP programs (macro and meso levels) are active. The macro-FEAP sends data to the meso-FEAP as input file prescribing the boundary conditions and waits until equilibrium is reached at the meso-level. Just after convergence the necessary data is treated and sent back in a file to the macro level which continues the computations.

In order to set the communication between macro and meso FEAPs and external application is performing as a MASTER program. In our case all programs are running in a LINUX environment and a *shell script* code constitutes the multi-scale mater program that triggers the calls to both macro and meso FEAPs.

Once all input files are prepared the master program calls macro FEAP at the beginning of the analysis. Macro FEAP runs normally until it reaches the element level. There information about a new boundary value problem is sent and macro computations are paused. The master program interprets the sent information and calls a meso FEAP with the input file of the corresponding meso mesh. When meso computations are finished data is sent back to the macro FEAP which jumps to form the quantities for the next element and the process is repeated. The master program is continuously searching for the details of the new meso cell in order to perform the call until an END file is sent from the macro FEAP indicating that the analysis has finished. Figure 2.4 illustrates the calling sequences and links between macro, meso and master programs during a two-scale analysis.

The following macro and meso input files show the main standard parts affected by the two-scale analysis. In the macro input file an initialization of the transformation matrices has to be done and, once in the solution module, elements have to be formed using the data exchange procedure. At the end of the meso input file, once convergence is reached, commands are found to form, condense and transform the stiffness matrix and RHS before they are sent back to the macro level.

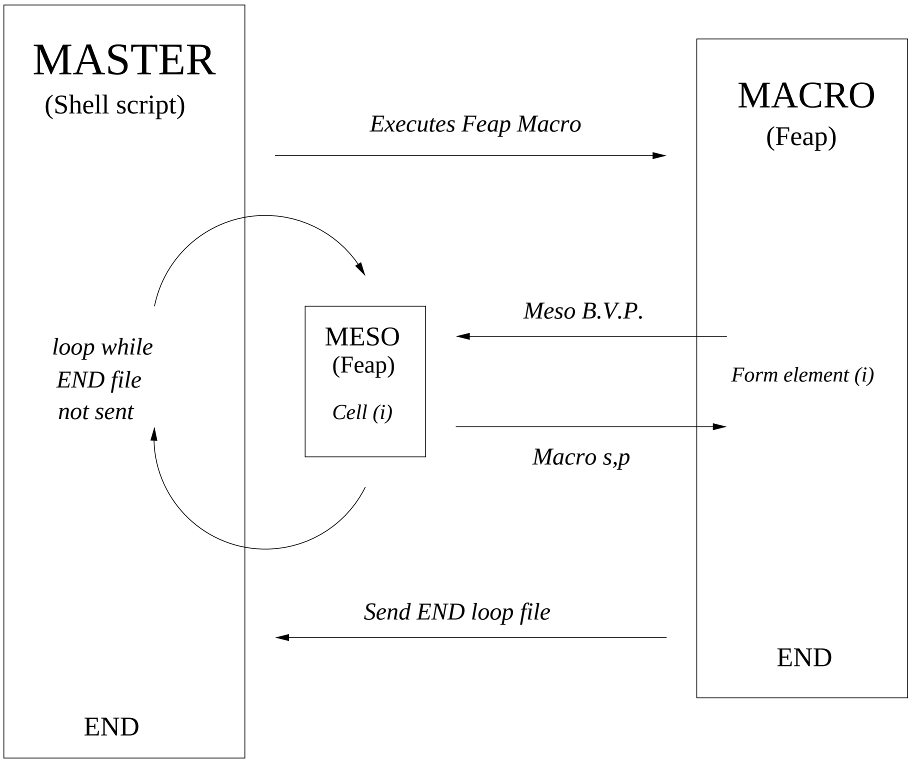
MASTER
(Shell script)
Executes Feap Macro
MACRO
(Feap)
loop while
END file
not sent
MESO
(Feap)
Cell (i)
Meso B.V.P.
Form element (i)
Macro s,p
Send END loop file
END
END

Figure 2.4: Two-scale framework implemented scheme. Communication between master, macro and meso programs.

Macro input file

```
FEAP !3 element macro-level test
8, 3, 1, 2, 2, 4

INCL,IMACR.msh
INCL,IMACR.bou

MATErial,1!,MATRIX
SOLI
ELASTIC ISOTROPIC 25000.0 0.2
PLANe STRAIN
QUAD DATA 2 2
END

BATC
MULT,MACRO_INIT !Initialize Transformation matrices
TOL,,1.d-6
PROP,,1
DT,,1/1
LOOP,time,1
TIME
LOOP,iter,10
! PENL !Penalty approach
MULT,MACRO_FORM !Form macro-element quantities
UTANG
FORM
SOLV
next,iter
next,TIME
PLOT,WIPE
plot,mesh
plot,disp
FDPL,,1,6.0,0
MEND
END

2,2
0.0,0.0 0.1,1.0


INTE

STOP
```

Meso input file

```
FEAP ! Irregular very fine mesh with pore
372, 638, 1, 2, 2, 3

INCL,Im002.msh

MATErial,1!,MATRIX
SOLI
ELASTIC ISOTROPIC 25000.0 0.2
PLANe STRAIN
QUAD DATA 2 2
END

BATC
TOL,,1.d-6
RESTART
MULT,MESO_INIT !Initialize s,p
PROP,,1
DT,,1
LOOP,time,1
TIME
LOOP,iter,10
PENL
UTANG
FORM
SOLV
next,iter
PLOT,WIPE
plot,mesh
plot,disp
next,TIME
CNDS !triggers order to condense
UTANG !assemble stiffness and condense
FORM !assemble rhs vector and condense
SAVE
END

INTE

STOP
```

The script file of the master program is also shown. The parts in which macro and meso FEAP are called are briefly commented.

```
#!/bin/csh -f
echo ””
echo ””
echo ””
echo ””
echo ”========================================”
echo ”                    Running Multi-scale Analysis”
echo ”========================================”

# remove old files
\ rm MACRO.END
\ rm MESO_IFILE
\ rm Rm*
\ rm MACRO_CONV.dat
\ cp feapname.macro feapname
../../../feap ¡¡ EOD ¿& macro.log &
y
EOD

# Main loop (while END file is not sent)
echo ””
echo ”Running Macro”
echo ””

while ( ! -e MACRO.END )
sleep 0.3

# Check macro-convergence file and
# display it
if ( -e MACRO_CONV.dat ) then
echo ””
cat MACRO_CONV.dat
echo ””
\ rm MACRO_CONV.dat
endif

# Read file containing name of meso-
# cell to process and execute FEAP with the corres
# ponding input file
if ( -e MESO_IFILE ) then
set NMES=‘cat MESO_IFILE‘
cat MESO_IFILE — awk ’s=substr($1, 2, length($1) - 1 ); print ”I”s” O”
s” R”s” R”s” P”s;’ ¿ feapname
cat feapname.tail ¿¿ feapname
\ rm MESO_IFILE
echo ”running meso ”$NMES
../../../feap ¡¡ EOD ¿& meso.log
y
EOD
endif
end

echo ””
echo ”========================================”
echo ”                    End of Multi-scale Analysis”
echo ”========================================”
echo ””


# last line
```

2.2.2 Particular implementation issues

In this section some comments are given about particular details of the multi-scale implementation in a FE package.

The Penalty Method

A crucial part of the implementation resides on the explicit matrix operations performed to the system of equations at the meso level. Equations (2.6) to (2.11) summarize all manipulations performed to the partitioned mesostructural system. It is also known that in a standard FE code all prescribed degrees of freedom (i.e. *essential* or *Dirichlet* type boundary conditions) are automatically eliminated from the system. A reduced system can be formed containing all free degrees of freedom together with a modified right hand side in which the effect of the constraints is taken into account. Considering that the framework follows a strain driven formulation the constraints are of *essential* type and, for this reason, another methodology is needed to prescribe the boundary conditions and keep the full structure of the system at the same time.

The *penalty method* is chosen for this purpose in the present implementation. It can be seen as a method to impose multifreedom constraints [1] [4]. In the present case all boundary nodes of the meso-specimen are prescribed with a non zero value (case of *single-freedom non-homogeneous multifreedom constraint.* Hence, when the penalty method is used to prescribe the boundary conditions at the meso level equation (1.14) can be rewritten as follows:

$$\begin{bmatrix} \boldsymbol{K}_{pp} + \omega & \boldsymbol{K}_{pf} \\ \boldsymbol{K}_{fp} & \boldsymbol{K}_{ff} \end{bmatrix} \begin{bmatrix} \boldsymbol{u} \\ \boldsymbol{u}_f \end{bmatrix} = \begin{bmatrix} \boldsymbol{f} + \boldsymbol{u}_p \cdot \omega \\ \boldsymbol{f}_f \end{bmatrix}, \tag{2.12}$$

where the constrained nodal displacements $\boldsymbol{u}$ are now treated as unknowns. The prescribed values $\boldsymbol{u}_p$ are affecting the right hand side of the system and a new scalar variable ω is introduced which sets the weight or intensity to impose the constraint. Hence the constraint is not imposed exactly and the error depends on the chosen weight. Increasing the weight leads to a more exact boundary prescription however the system of equations becomes bad conditioned. In order to find a balance between the two cases the value of the penalty weight can be found according to $\omega = 10^k\sqrt{10^p}$ (see [4]), where k is the order of the highest diagonal coefficient of the stiffness matrix and p is linked to the working precision of the machine.

Matrix storage and explicit matrix operations

In order to perform all matrix manipulations (2.6) to (2.11) the use of an optimal storage scheme seems necessary. The FE package FEAP uses a symmetric profile storage (*skyline*) of the stiffness matrix (see [29]). Diagonal, upper and lower coefficients of the stiffness matrix are stored in three separate arrays. The upper non-zero coefficients are stored by columns and the lower ones are stored by rows using an auxiliary pointer array that specifies the correct location. A significant reduction of the storage is found using this technique.

---

[1] Multifreedom constraints (MFC) can be defined as functional equations that connect two or more displacement components.

In the current implementation all matrix operations are performed explicitly over fully stored matrices. This academical implementation of the framework reduces considerably the size of the problems that can be tackled. On the other hand it is chosen as a preliminary implementation because of its potential to solve questions about the future field applicability of the implementation.

Special mention has to be done on the chosen matrix condensation procedure. The formulation shown in (2.8) and (2.9) clearly involves the inversion of a large matrix. From a computational point of view this operation is considered extremely expensive and one should avoid it when large systems need to be processed. An alternative can be the calculation of any of the rectangular matrices

$$\boldsymbol{K}_{pf}^{m,e}(\boldsymbol{K}_{ff}^{m,e})^{-1} \; or \tag{2.13}$$

$$(\boldsymbol{K}_{ff}^{m,e})^{-1}\boldsymbol{K}_{fp}^{m,e} \tag{2.14}$$

columnwise via the successive solutions of the corresponding system. For example, if the rectangular matrix

$$\boldsymbol{K}_{fp}^{rec} = (\boldsymbol{K}_{ff}^{m,e})^{-1}\boldsymbol{K}_{fp}^{m,e} \tag{2.15}$$

is chosen to be computed, the system:

$$\boldsymbol{K}_{ff}^{m,e}(\boldsymbol{K}_{fp}^{rec})_j = (\boldsymbol{K}_{fp}^{m,e})_j \tag{2.16}$$

needs to be solved for all columns $j = 1 \cdots p$.

It can be proved that this alternative condensation procedure is p times more expensive than a normal solution of our system of equations. This can represent a significant advantage when the number of constrained degrees of freedom is remarkably low (in case of periodic boundary conditions). In the case that a direct solver with a triangular decomposition method is used, the decomposition is done only once and the solution vectors are successively computed varying the corresponding RHS.

In the computer implementation of the static condensation process calculations are normally carried out using *Gauss Elimination*. In this procedure the free degrees of freedom are sequentially being eliminated from the system using row and column operations. When the system contains thousands to milions of dofs the elimination procedure is carried out using more sophisticated techniques [3].

In the present implementation the partition of the stiffness matrix containing interior degrees of freedom is inverted explicitly. The extension to a more optimized way of dealing with matrix manipulations is being considered for an upcoming version.

Chapter 3

Performance examples

In this section the implemented framework is tested for an elastic, plastic and a gradient damage model. In order to assess the performance of the framework different examples are carried out and compared to a mono-scale analysis solution.

3.1 Linear Analysis

3.1.1 Bar under uniaxial loading

In this example a uniaxial loading test is imposed to a bar composed by three Q4 elements (Figure 3.1). The bar is submitted to uniaxial loading and the center element is modeled at a meso-level using two different T3-element discretisations as depicted in Figure 3.2. The material is modeled elastic with Young's modulus $E = 25 \times 10^3 N/mm^2$ and Poisson ratio $\nu = 0.2$ at the meso-level and at macro-elements in which no multi-scale analysis is performed.

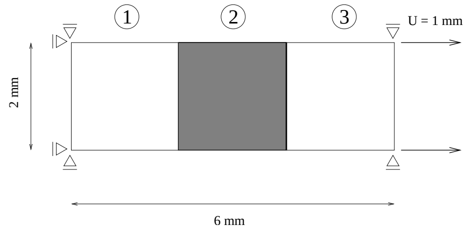

Figure 3.1: Bar under uniaxial loading.

Figure 3.3 shows a force displacement plot at the vertical right boundary of the macro-level when mono-scale and multi-scale analyses (using both discretisations) are performed. The solution field at the macro-level turns out to be identical when the mono-scale analysis is compared to the multi-scale one using a homogeneous discretisation. This result is translated in the force displacement plot where the resulting curves overlap each other. The behaviour of the discretisation with void inclusions deviates from the homogeneous

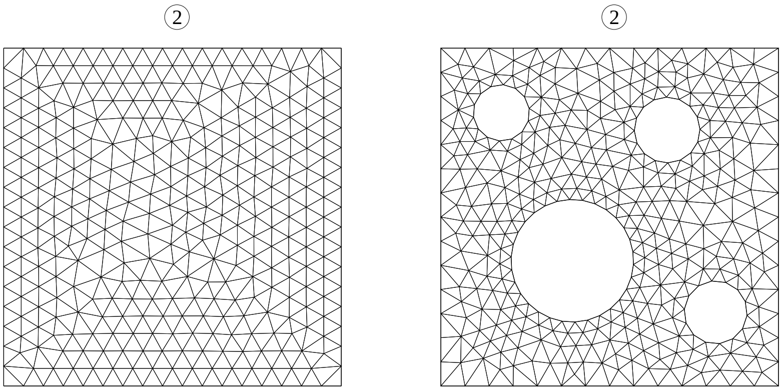

Figure 3.2: Left: Homogeneous discretisation (694 dofs). Right: Discretisation with void inclusions (804 dofs).

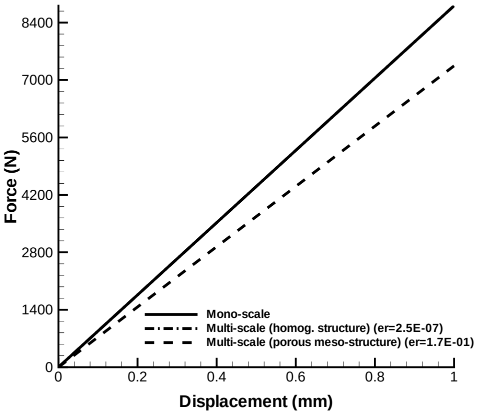

Figure 3.3: Force vs displacement plot at the right boundary.

one showing a predictable weaker response.
Displacement contours are shown in Figure 3.4 for both macro and discretisations.

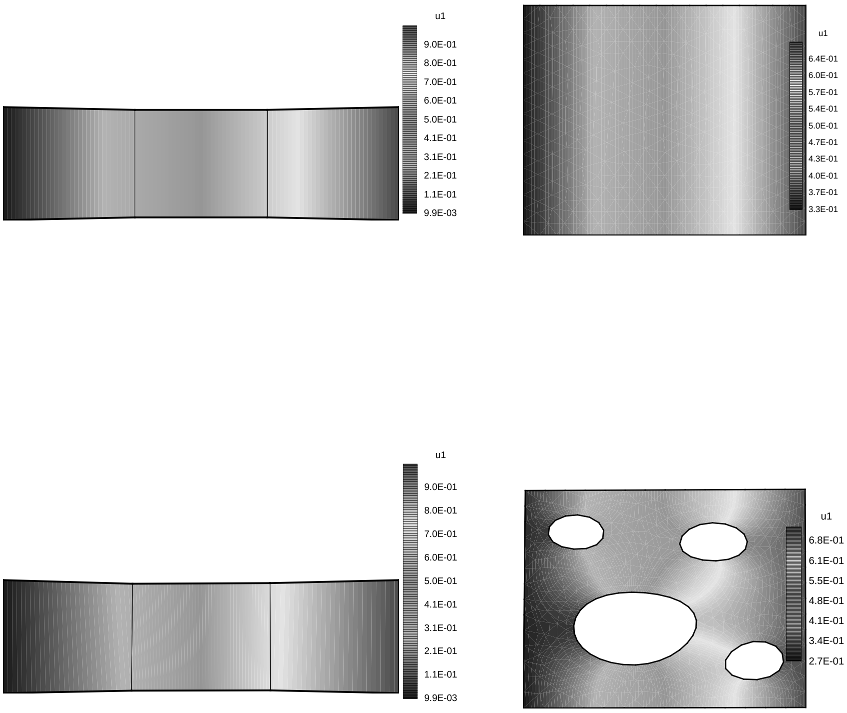
u1
9.0E-01
8.0E-01
7.0E-01
6.0E-01
5.0E-01
4.1E-01
3.1E-01
2.1E-01
1.1E-01
9.9E-03
u1
6.4E-01
6.0E-01
5.7E-01
5.4E-01
5.0E-01
4.7E-01
4.3E-01
4.0E-01
3.7E-01
3.3E-01
u1
9.0E-01
8.0E-01
7.0E-01
6.0E-01
5.0E-01
4.1E-01
3.1E-01
2.1E-01
1.1E-01
9.9E-03
u1
6.8E-01
6.1E-01
5.5E-01
4.8E-01
4.1E-01
3.4E-01
2.7E-01

Figure 3.4: Horizontal displacement contours (mm) at the macro-level (left) and meso-level (right) for the first (top) and second (bottom) discretisation.

3.1.2 Bending test

Bilinear elements behave far too stiff in bending and for this reason a coarse macro-mesh should not be used at the macro-level when comparing the homogeneous multi-scale solution to the mono-scale one. For this reason a reduced integration scheme for this element type is proposed.

Another alternative is to refine the macro mesh as shown in the following bending example (Figure 3.5). A meso-scale analysis is only performed to the shaded element. Figure 3.6 shows the different discretisations adopted for the analysis. Material properties are assumed to be identical to the ones used in the previous example except for the last porous discretisation which is designed to be weaker with Young's modulus $E = 200N/mm^2$ and Poisson ratio $\nu = 0.4$. Vertical displacement contours are shown in Figure 3.8. A force displacement plot of the node where the load is applied is presented in Figure 3.7. The behaviour of the first and second meso-discretisations compared to the monoscale analysis is similar in this case. This makes sense for the homogeneous discretisation which hardly deviates from the mono-scale response and presents a relative error in the vertical displacement of the order 10^{-4}. Although in this particular case, the porous structure is not weak enough to produce a notorious change in the mechanical response but it can be seen that the relative error in displacement increases towards 10^{-2}. When a weaker material assigned to this cell (third meso-structure) a different displacement contour plot can be observed both at macro and meso levels (Figure 3.8 bottom) and its effect is directly seen in the force displacement plot Figure 3.7.

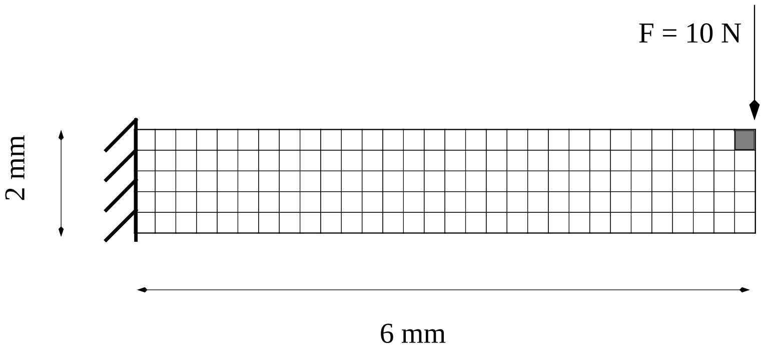

Figure 3.5: Macro mesh for the bending test.

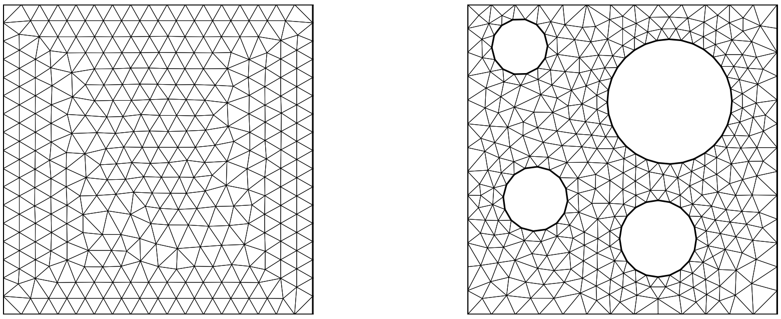

Figure 3.6: Left: Homogeneous discretisation (696 dofs). Right: Discretisation with void inclusions (762 dofs).

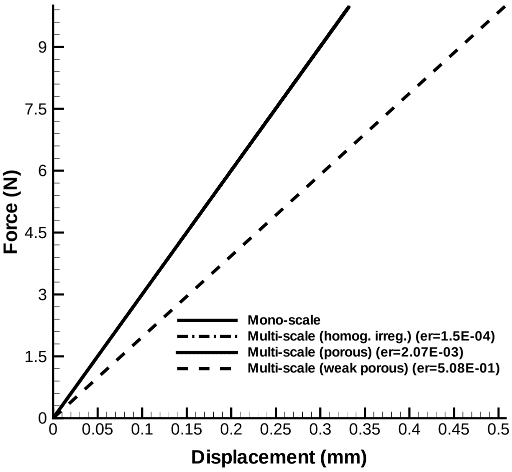

Figure 3.7: Force vs displacement plot at the top right node.

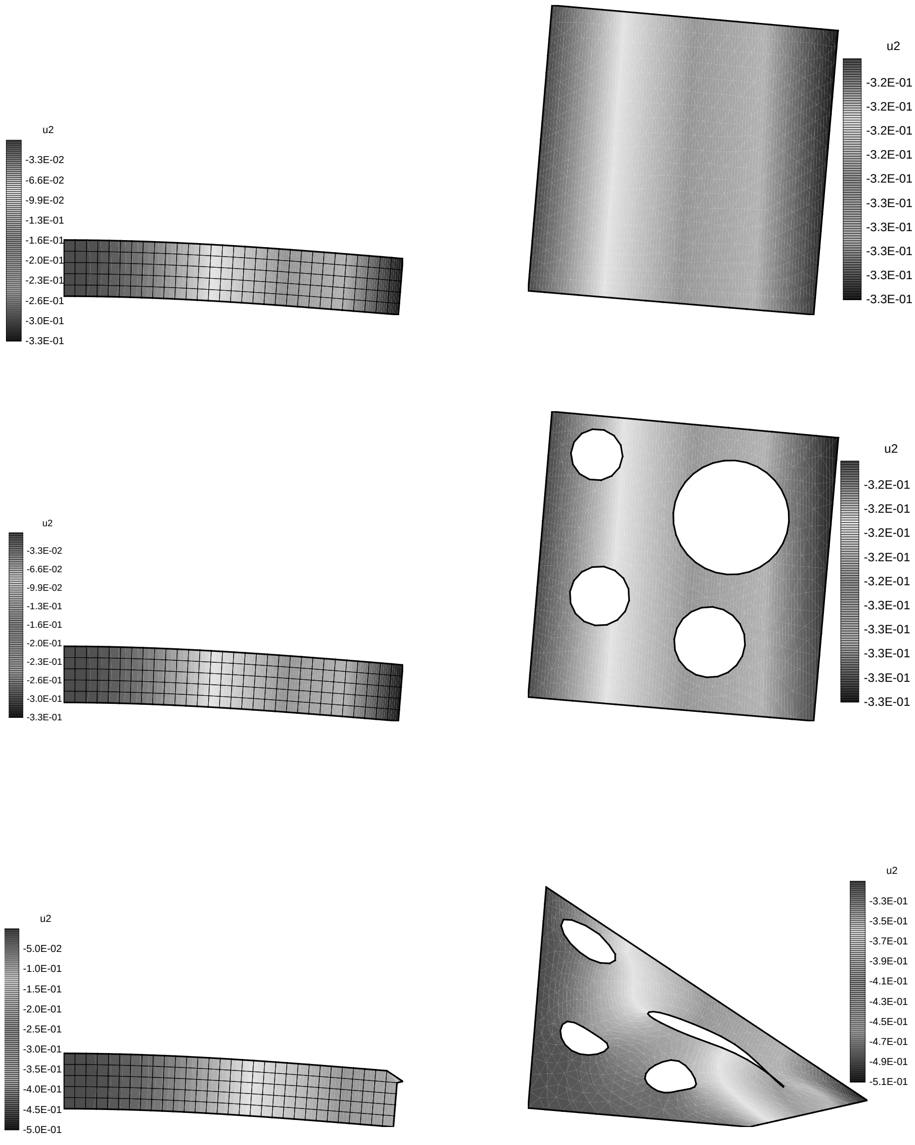

Figure 3.8: Vertical displacement contours (mm) at the macro-level (left) and meso-level (right) for the homogeneous (top), porous (middle) and weak porous (bottom) discretisation.

3.2 Non-linear examples

3.2.1 Bar under uniaxial loading

In order to test the framework in a non-linear context the following example has been carried out. The test is summarized in Figure 3.9. All macro elements have a corresponding meso-discretisation. Two meso-discretisation sets have been used and they are summarized in Figure 3.10.

An elasto-plastic model (3.1) is used with the following parameters: Young's modulus and Poisson ratio are set to $E = 50000N/mm^2$ and $\nu = 0.0$, respectively. The uniaxial yield stress $\Upsilon_0 = 200N/mm^2$, the stress at large values of strain $\Upsilon_\infty = 400N/mm^2$, and the delay constant $\beta = 10^3$.

$$\Upsilon(\boldsymbol{\epsilon}^{pl}) = \Upsilon_\infty + (\Upsilon_0 - \Upsilon_\infty)\, e^{(-\beta \boldsymbol{\epsilon}^{pl})} \tag{3.1}$$

The force displacement plot shown in Figure 3.11 shows that the discretisation with a void structure in the middle cell behaves much softer than the rest. When comparing the mono-scale response with the homogeneous discretisation the curves coincide completely. The displacement distributions for both discretisation sets are depicted in Figures 3.13 and 3.14. It can be seen that the void structure creates a heterogeneous displacement field which is reflected at the macro-level. The meso displacement contours can be compared to the mono-scale contours depicted in Figure 3.12. Stress contours for discretisations A and B are also shown in Figures 3.13 and 3.14. It can be observed that the stress distribution for discretisation set A shows spurious fluctuations that should not be considered due to the fact that the upper and lower limits of the plotted stress are exactly the same, hence the stress is constant all over the cell as well as in the mono-scale analysis. Discretisation B shows a different stress distribution caused by the heterogeneous void structure.

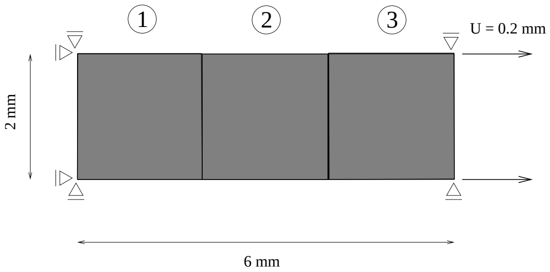

Figure 3.9: Uniaxial test for the multi-scale non-linear analysis

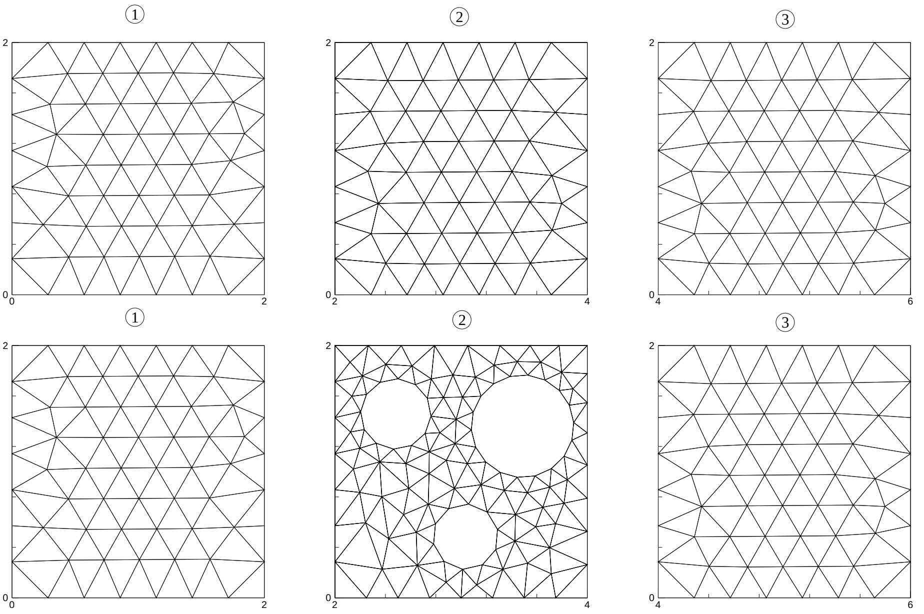
①
②
③
2
0
0
2
2
0
2
4
2
0
4
6
①
②
③
2
0
0
2
2
0
2
4
2
0
4
6

Figure 3.10: Top: Homogeneous meso-structure discretisation (set A: around 134 dofs) . Bottom: Void meso-structure discretisation (set B: 252 dofs for void discretisation).

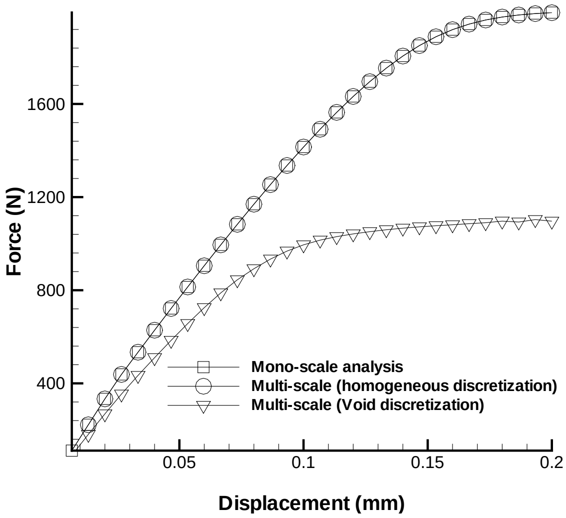

Figure 3.11: Force displacement plot at the right boundary

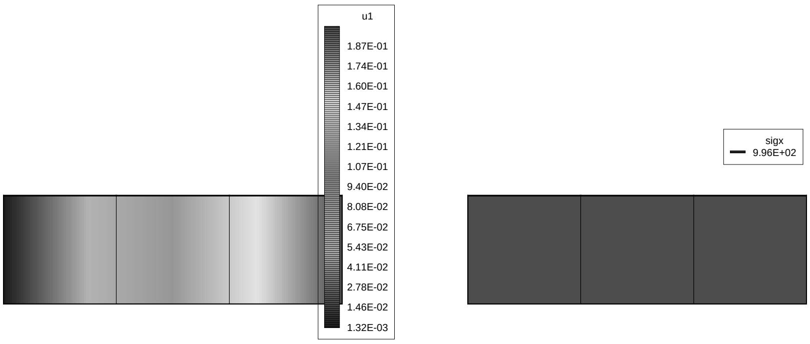

Figure 3.12: Mono-scale horizontal displacement contours (Left) and horizontal stress contours (Right)

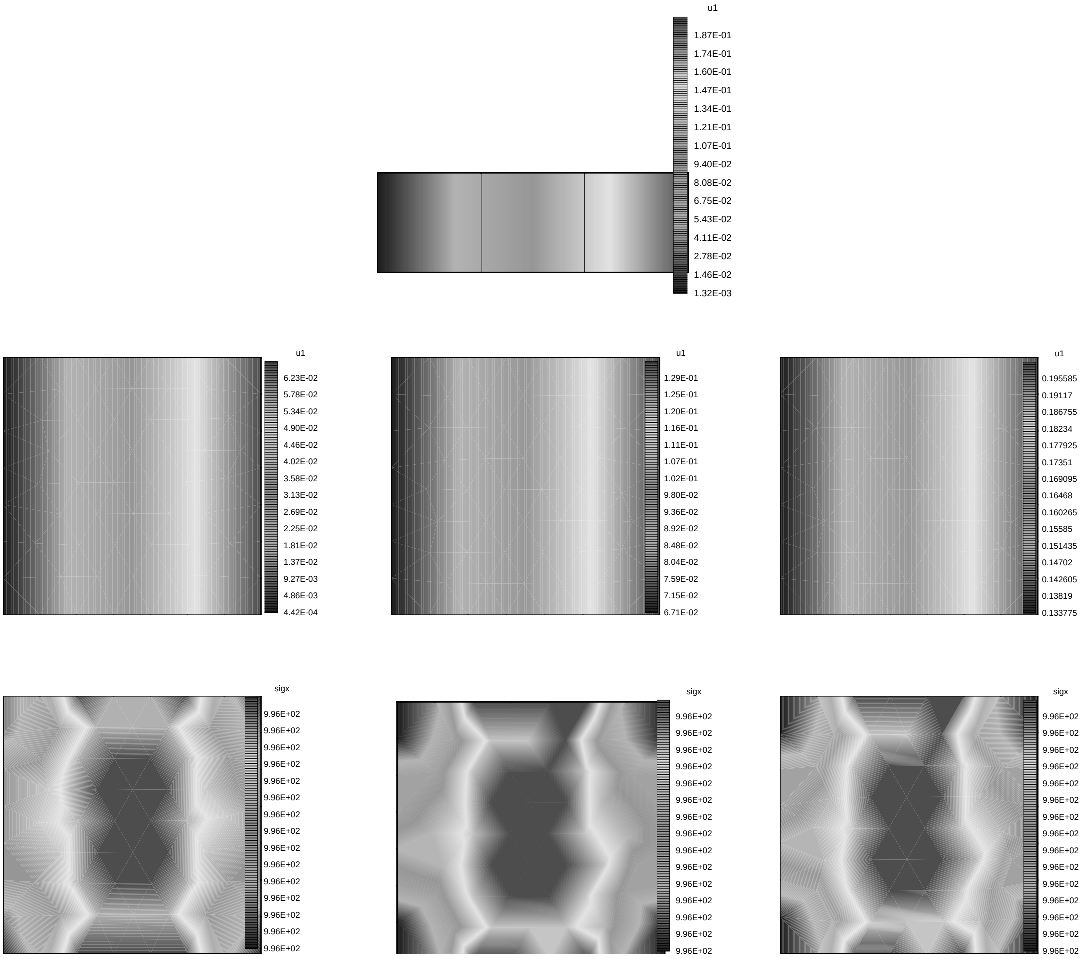

Figure 3.13: Horizontal Displacement contours for the macro-level structure (top) and meo cells (middle) corresponding to discretisation set A. Horizontal stress contours for discretisation set A (bottom)

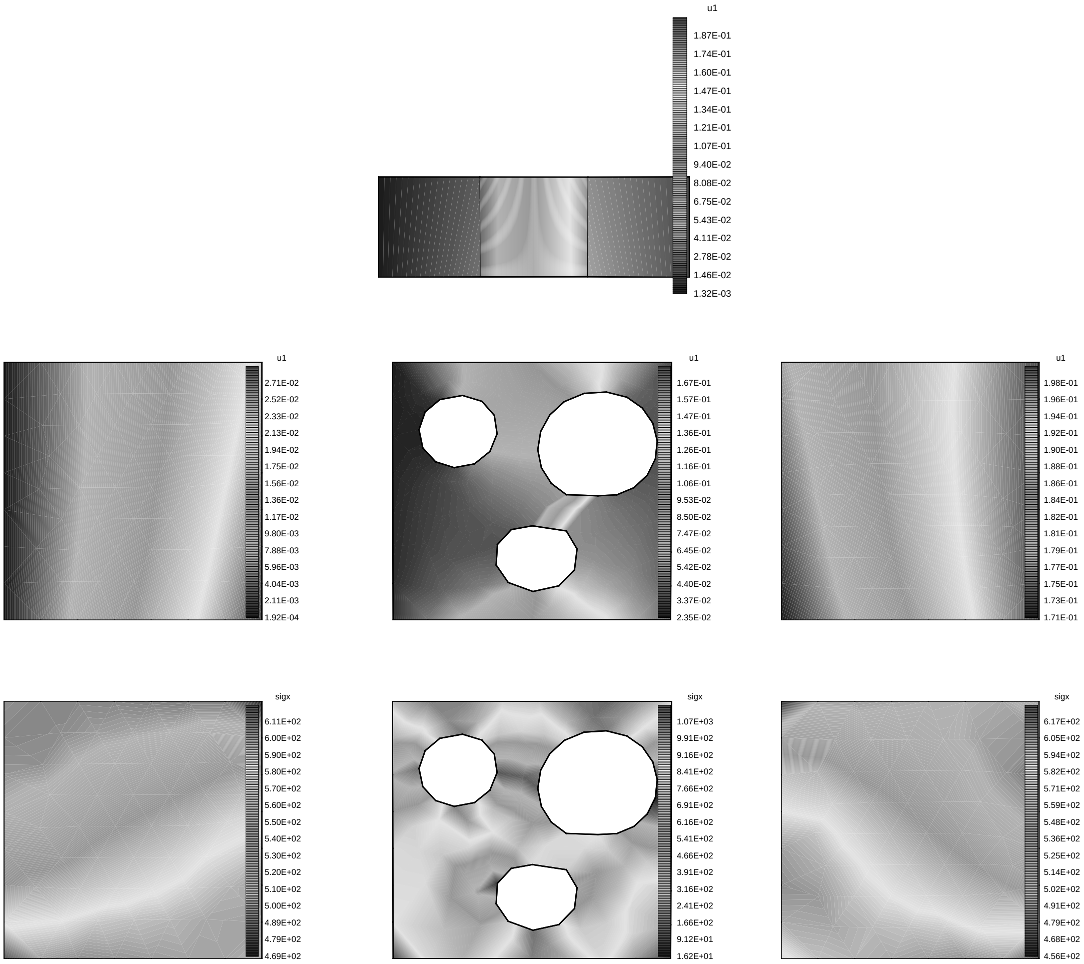

Figure 3.14: Horizontal Displacement contours for the macro-level structure (top) and meso cells (middle) corresponding to discretisation set B. Horizontal stress contours for discretisation det B (bottom)

3.3 Framework extension for the gradient enhanced damage model

The assessment of the implementation for models that allow for softening and localisation is the main goal of this study. The gradient enhanced damage model (see appendix A) is considered at the meso level as a constitutive model that accomplish the former requirements. An extension to the previous framework formulation is needed in order to allow the implementation to deal with models containing extra degrees of freedom. The gradient damage model considers a third degree of freedom (the non-local equivalent strain) in its formulation as a result of a coupling between the equilibrium and the gradient enhancement equations. When the mesoscopic stiffness matrix is assembled all extra degrees of freedom are stored in the submatrices $\boldsymbol{K}_{ff}$, $\boldsymbol{K}_{pf}$ and $\boldsymbol{K}_{fp}$ (see (2.6)) together with the rest of internal unknowns. Special care must be taken with those extra degrees of freedom belonging to a boundary nodal point. In this case the first two unknowns are assembled with the prescribed degrees of freedom and the extra unknown is considered free. After the condensation procedure all internal unknowns (including the extra degrees of freedom) are eliminated from the system and information related only with displacement unknowns is sent up to the macro level. The upscaling of the third degree of freedom is not considered in the present approach.

3.3.1 Performance of the framework for a simple localisation test

The necessary parts of the framework are extended in order to be able to deal with specific constitutive models including extra degrees of freedom such as the gradient damage model. The meso-structure studied in this case is depicted in Figure 3.15. The first test (monoscale) is performed directly to the mesh using the boundary conditions depicted in Figure 3.16. The second test is performed using the multi-scale framework to a macro-structure composed by a single quad which has the meso-structure shown in Figure 3.15. The boundary conditions imposed to the macro-element are shown in Figure 3.16. A gradient damage model is used for both materials with the following parameters: Young's modulus is set to $E = 150000 N/mm^2$ and $E = 25000 N/mm^2$ for the matrix and weak inclusions, respectively. The Poisson ratio is set to $\nu = 0.0$ for both materials. The rest of the parameters are set to be equal for both materials: the parameter related with the internal length scale $c = 0.2 mm^2$, initial strain $k_0 = 0.05$, the parameters for the exponential softening law $\alpha = 0.9$ and $\beta = 50$.

Comparing Figures 3.17 and 3.18 it can be seen that, due to the linear displacements imposed to the meso-specimen, localisation cannot take place at the boundary. For this reason the meso specimen is behaving stiffer and more ductile than the natural response shown in the mono-scale test. A load displacement graph is provided for both analyses in Figure 3.19. It can be observed that the multi-scale test dissipates more energy. For this reason the boundary conditions adopted to transfer the displacements from the macro to the meso level do not seem to be adequate for localisation problems.

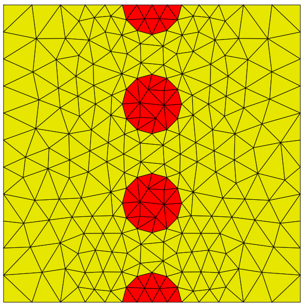

Figure 3.15: Meso-discretisation with weak inclusions.

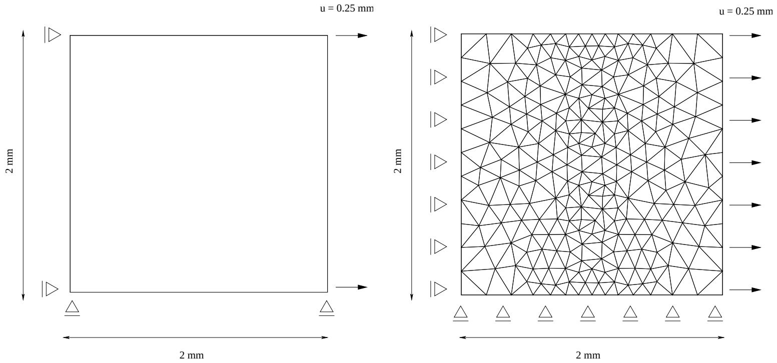

Figure 3.16: Boundary conditions imposed to the macro-element in the multi-scale analysis (left) and meso structure for the mono-scale analysis (right).

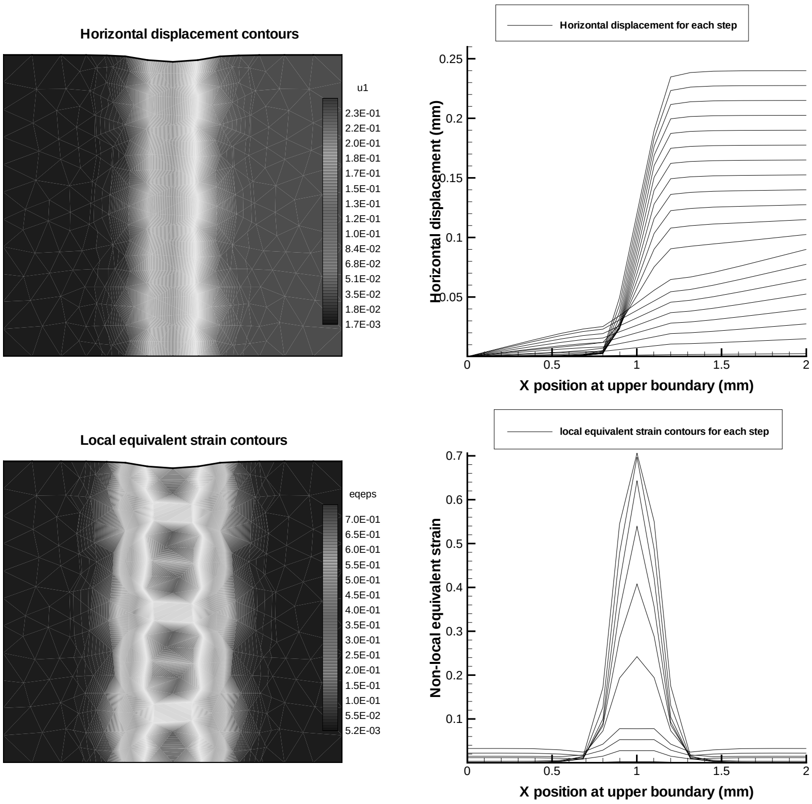

Figure 3.17: Mono-scale analysis. Top to bottom: Displacement contours (left) and displacement profiles at the upper boundary (right), local equivalent strain contours (left) and local equivalent strain profiles at the upper boundary (right).

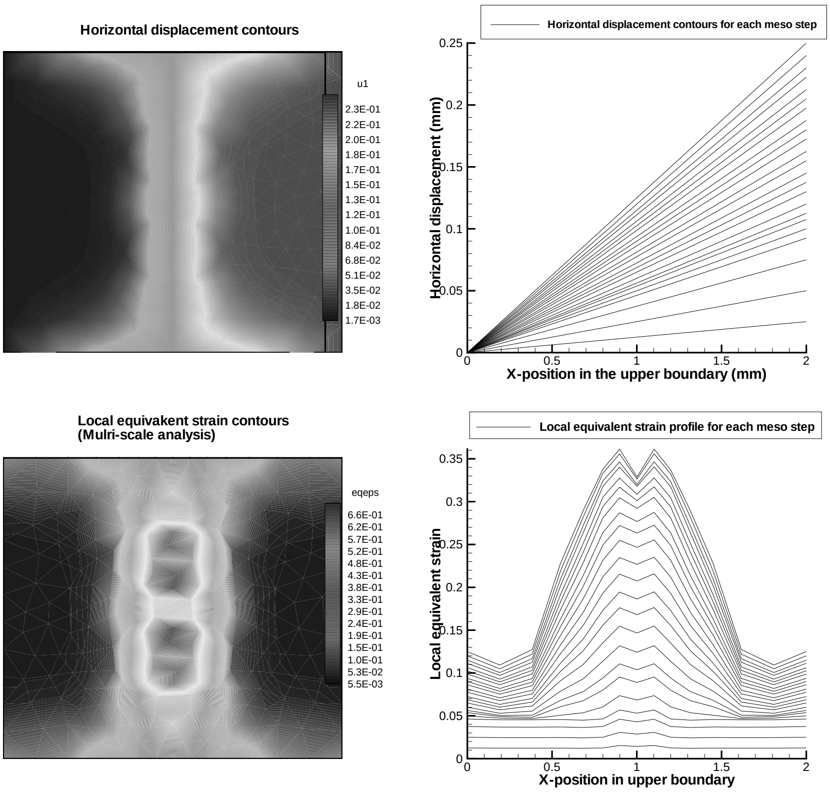

Figure 3.18: Multi-scale analysis. Top to bottom: Displacement contours (left) and displacement profiles at the upper boundary (right), local equivalent strain contours (left) and local equivalent strain profiles at the upper boundary (right).

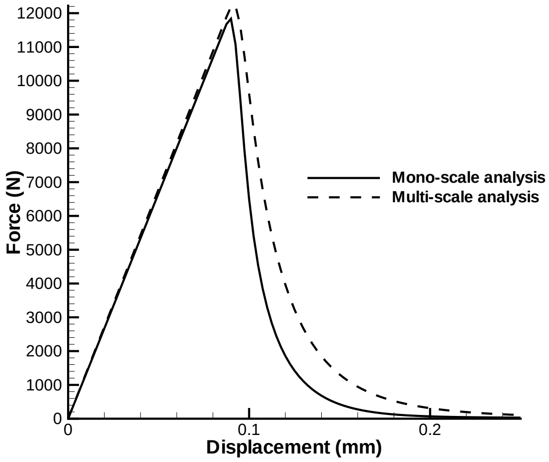

Figure 3.19: Force displacement graph for mono and multi-scale analysis.

3.3.2 Performance of the framework for more complex localisation tests

In this section a localisation test is performed on a specimen with void inclusions. The body contains three voids aligned diagonally and is loaded vertically in tension (Figure 3.20). Figure 3.20 shows the structure of the specimen. A gradient damage model is used with the following parameters: The Poisson ratio is set to $\nu = 0.2$. The parameter related with the internal length scale $c = 0.25mm^2$, initial strain $k_0 = 0.05$, the parameters for the exponential softening law $\alpha = 0.999$ and $\beta = 7.0$. The light-shaded area in Figure 3.20 is meant to behave weaker than the rest with Young's modulus $E = 2500N/mm^2$ and $E = 25000N/mm^2$, respectively. With these set of parameters the void contained in the light-shaded area damages first and then the localised zone propagates through the rest of the voids in the direction of the pore alignment. The same test is performed to the macromesh shown in Figure 3.21. The mono-scale analysis predicts the correct response and it can be seen (Figure 3.22) how strain localizes through all three voids. The multi-scale analysis fails when predicting the localisation pattern. Due to the linear boundary conditions used to transmit the data between macro element edges, a diagonal distribution of strain in meso-specimens is not feasible. For this reason damage can only propagate horizontally in this test providing an incorrect failure mechanism.

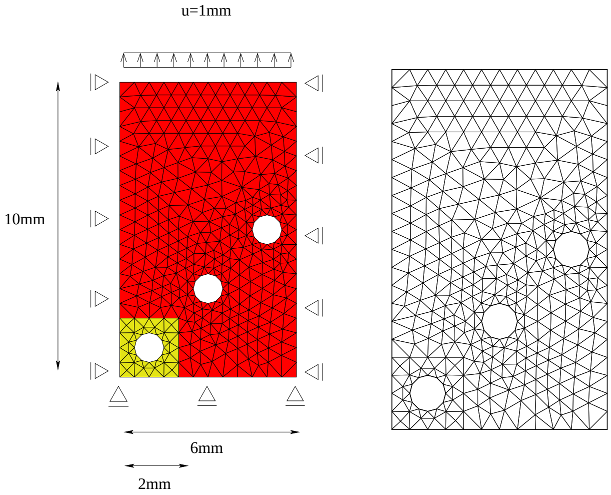

Figure 3.20: Tensile test for the porous structure (left) and mono-scale analysis discretisation (right).

The global response of the body is analysed at the top boundary for the multi and mono-scale cases. The response of the multi-scale test turns out to be much more brittle (Figure 3.23). This is due to the unrealistic orientation of localisation caused by the chosen boundary contitions. Strain is localizing at the bottom of the specimen in a lower area compared to the mono-scale test. For this reason there is proportionally a larger area that downloads elastically during softening and for that provides a much more brittle behaviour of the specimen.

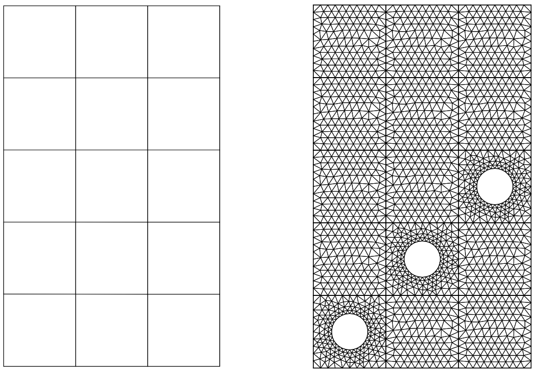

Figure 3.21: Multi-scale analysis discretisation. Macro-mesh (left) and corresponding meso-discretisations (right).

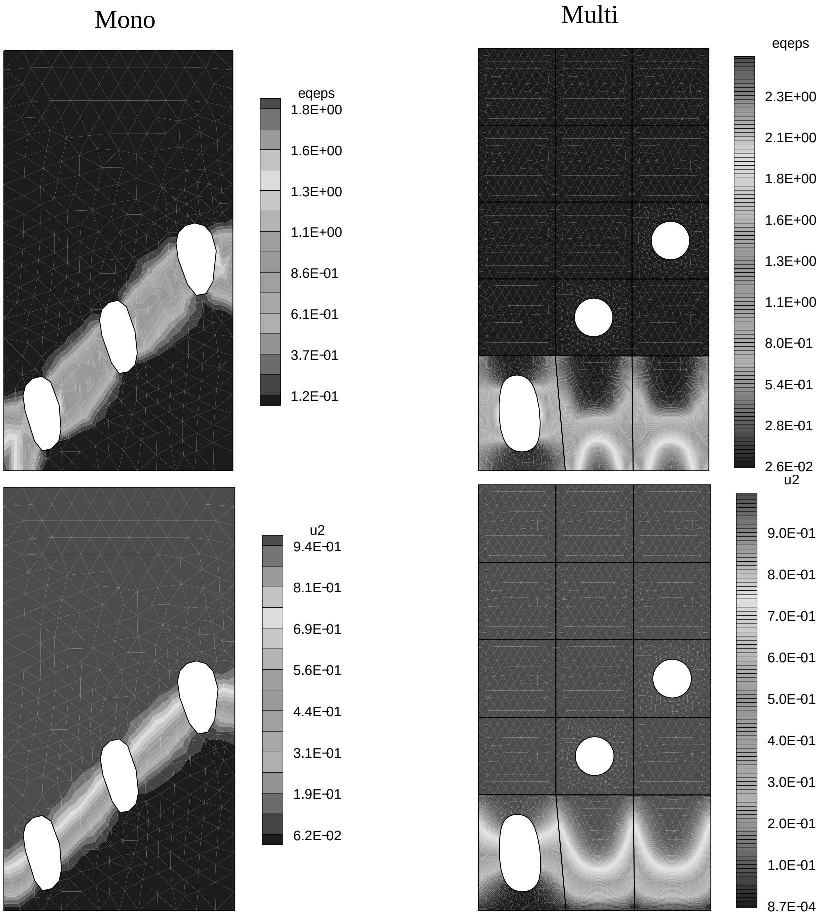

Figure 3.22: Left to right: contour plots for the mono-scale and multi-scale tests. Top to bottom: Equivalent strain and vertical displacement (mm) contour plots.

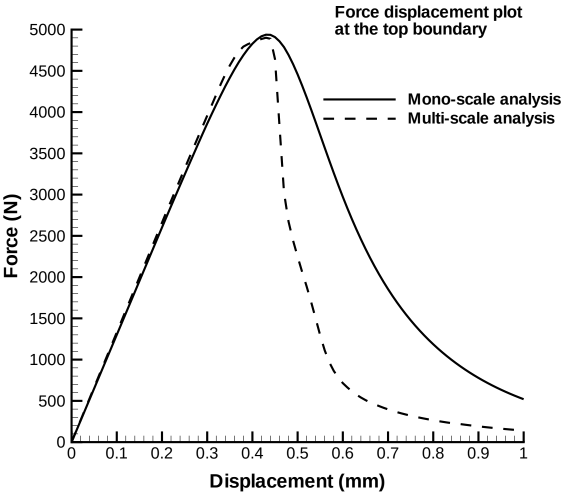

Figure 3.23: Force displacement plot for multi and mono-scale tests.

Chapter 4

Framework validation

4.1 Effect of the mesh discretisation

In order to make sure that the results are not dependent on the meso-discretisation, a similar test as described in the previous section is reproduced this time imposing a displacement $u = 0.2mm$ at the right boundary and using two different meso discretisations. Discretisation sets "A" and "A (fine)" are shown in Figure 4.1.

In this case an exponential hardening law is chosen (4.1) with the following parameters: Young's modulus and Poisson ratio are set to $E = 10000N/mm^2$ and $\nu = 0.2$ respectively. The uniaxial yield stress $\Upsilon_0 = 100N/mm^2$, the stress at large values of strain $\Upsilon_\infty = 500N/mm^2$, the isotropic hardening modulus $H_{iso} = 10^3N/mm^2$ and the delay constant $\beta = 10^2$.

$$\Upsilon(\boldsymbol{\epsilon}^{pl}) = \Upsilon_\infty + (\Upsilon_0 - \Upsilon_\infty)\, e^{(-\beta\boldsymbol{\epsilon}^{pl})} + H_{iso}\boldsymbol{\epsilon}^{pl} \tag{4.1}$$

The load displacement curves from both sets are identical to the mono-scale response as shown in Figure 4.2, hence the framework does not show a dependency on the meso-discretisation when modeling the same structure.

4.2 Effect of the step size

The dependency of the results on the step size is studied in this section. The same test as the one explained in the previous section is performed using mono-scale and multi-scale analysis on discretisation set A. Figure 4.3 shows the force displacement plots corresponding to mono-scale and multi-scale analysis for different number of steps. When comparing mono-scale with multi-scale responses, it can be seen that the difference increases when the step size is larger. This is, for larger steps the multi-scale analysis shows a deviation from the mono-scale one. The relative error between both responses can be at most of the order 10^{-2} for the largest step size computations and is decreasing during subsequent steps. A more accurate step discretisation shows almost no difference between mono and multi-scale computations. The maximum relative error between both responses is then lower than 10^{-3}.

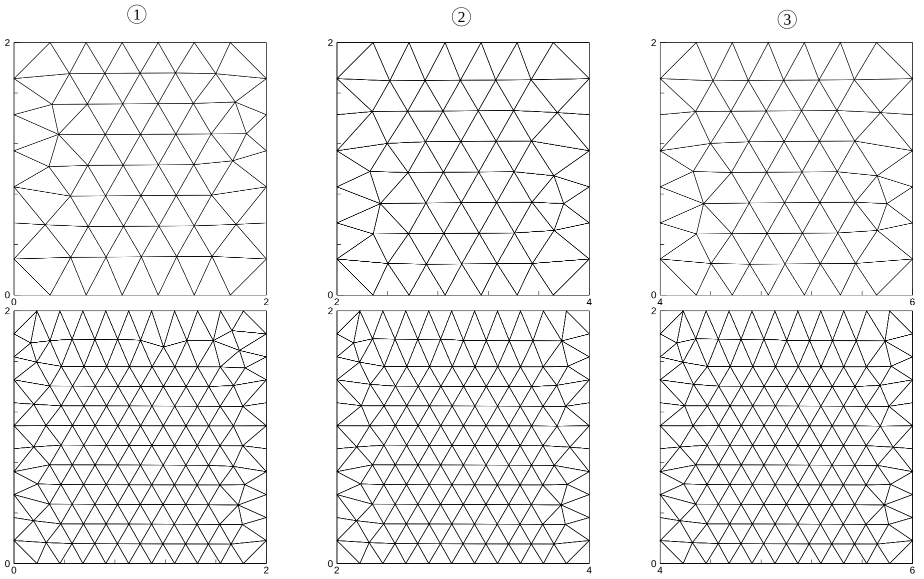

Figure 4.1: Discretisation sets A (around 134 dofs) (top) and A fine (around 300 dofs (Bottom).

4.3 Influence of the penalty method

The results from the previous sections manifest that the framework is independent of the meso-discretisation but shows a small dependency on the step size.

Considering that the constraints are not enforced exactly some small errors can arise during the multi-scale analysis. For this reason the penalty method is assessed in this section considering only mono-scale computations in order to facilitate the outcoming results.

The test depicted in Figure 4.4 is imposed to a bar using the same macro-discretisation as in the previous examples. An elasto-plastic model is again considered with exponential hardening and the same parameters as in Section 4.1.

Figure 4.5 shows the mechanical response using both standard boundary conditions and the penalty method when different steps sizes are chosen. It can be clearly seen that responses are slightly different when large step sizes (or fewer steps) are taken. The shapes of the relative error curves are similar to the ones observed in Figure 4.3. Hence, the penalty approach is most probable the source of the error detected in multi-scale computations when a large step size is considered. Moreover the error seems to magnify in multi-scale analysis because it can be, for the same problem, 10 times higher than the one observed with pure mono-scale computations using the penalty approach.

If we examine, for the 10 step case, the distribution of relative error for different values of the penalty weight in Figure 4.5 we can conclude that the penalty weight has a notorious influence on the results. Optimal values of the penalty weight (for this particular element size) are $w = 10^4$ and lead to the lowest relative error rates. When analyzing the relative errors obtained for different step sizes when using an optimal value of the penalty weight

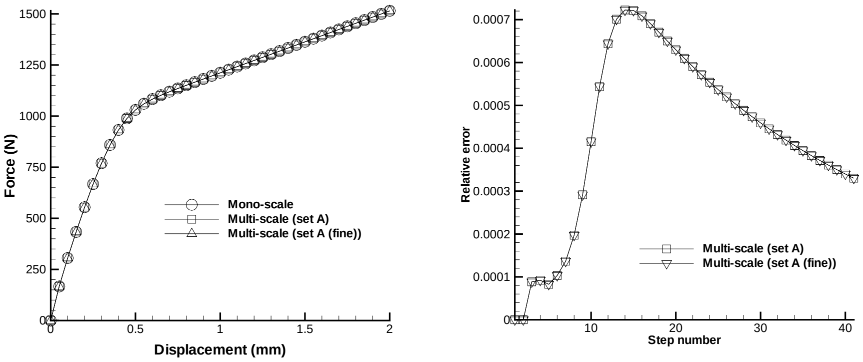

Figure 4.2: Left: Force displacement plots (set A and A fine). Right: Relative error plots for set A and A fine.

(Figure 4.5 bottom) the limits appear to be much lower and for that reason the method performs more accurately.

If we reproduce again the multi-scale test using an optimal value of the penalty parameter for the meso-computations we would obtain the force displacement and relative error graphics depicted in Figure 4.6. We can observe that there is not much improvement in the results when performing multi-scale analysis. The improvement was much better for the mono-scale cases in which the penalty method is employed.

The influence of the penalty weight on the multi-scale results for large step analysis is shown in Figure 4.7. It can be observed that for these steps sizes the penalty weight is not influencing the results.

In conclusion, it is not clear which is the cause of the error observed when comparing multi and mono-scale analysis for a coarse step discretisation.

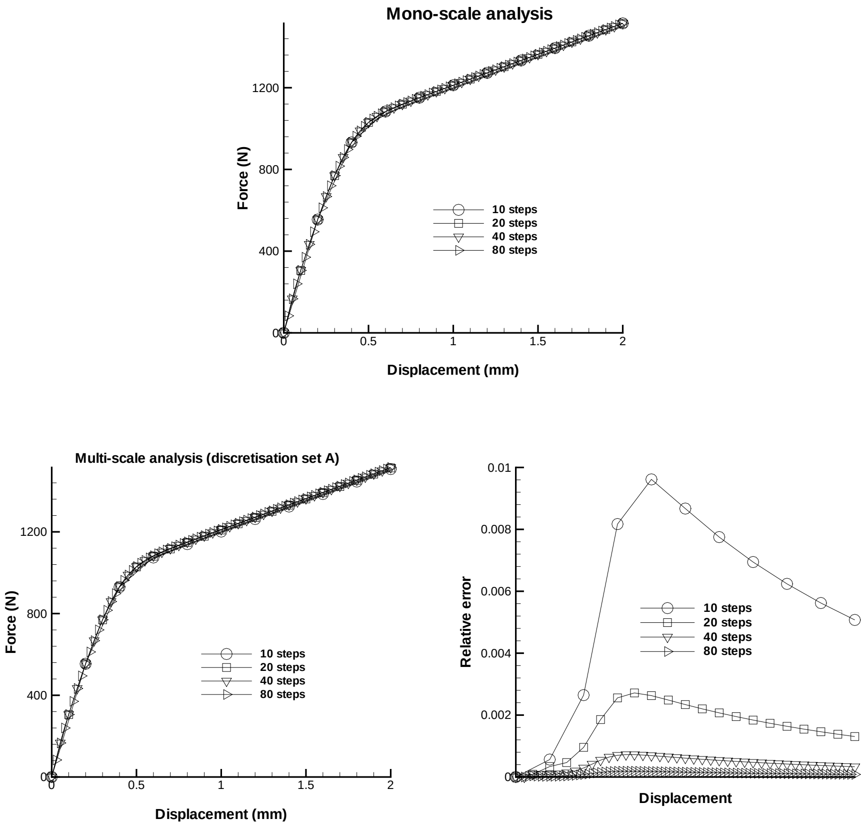

Figure 4.3: Step size dependency. Top: Mono-scale analysis force displacement plots. Bottom: Multi-scale analysis force displacement plots (left) and relative error (right).

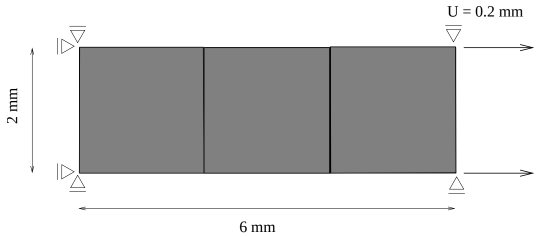

Figure 4.4: Uniaxial loading test.

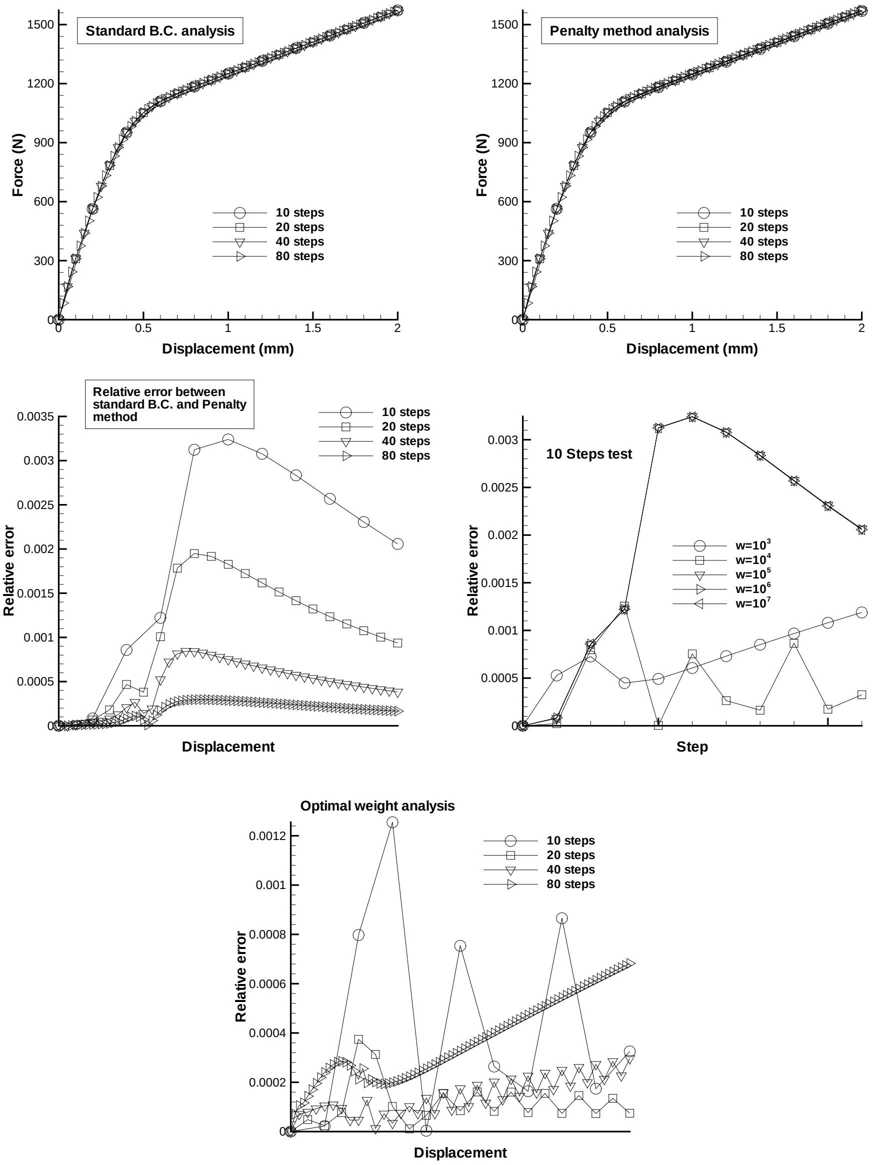

Figure 4.5: Top: Mechanical responses for standard b.c. (Left) and Penalty approach (Right). Middle: Relative error values between the two responses (Left) and 10 step analysis for different penalty weights. Bottom: Relative error values between the two responses for the optimal penalty weight.

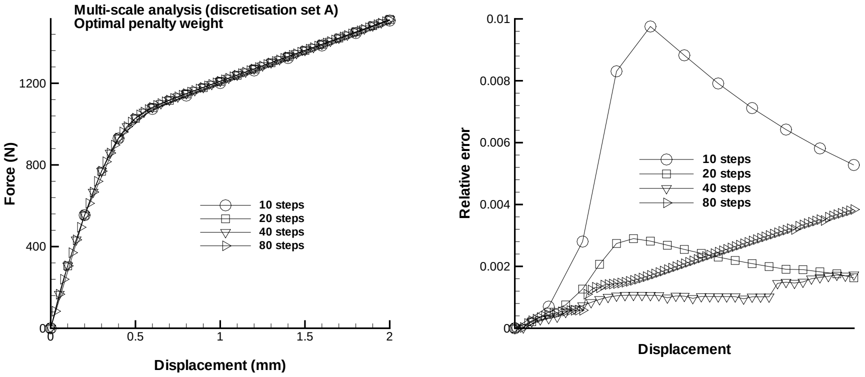

Figure 4.6: Step size dependency for optimal penalty weight. Left: Multi-scale analysis force displacement plots. Right: Relative error graphics.

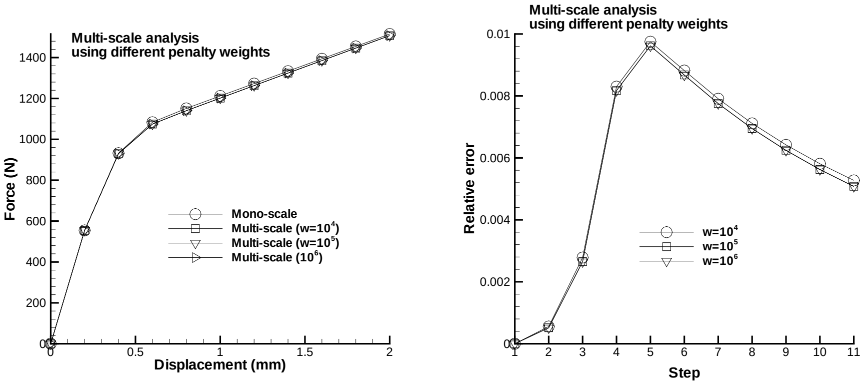

Figure 4.7: Penalty weight dependency for coarse step size discretisations in multi-scale analysis. Left: Multi-scale analysis force displacement plots. Right: Relative error graphics.

Chapter 5

Discussion and recommendations

A two-scale strong coupling method is implemented in this study. The method is supposed to deal with problems in which the scales are not separated [13].

An assessment of the implementation is carried out for an elastic, plastic and a gradient enhanced damage model (see appendix A).

When comparing the two-scale analysis computations with the corresponding analogous mono-scale tests a good agreement in results is found for the models that do not show softening. The linking between the scales allows the framework for macromesh and mesosize independence which are very important qualities for a reliable implementation. Up to this point the present implementation can be regarded not only as a tool to perform computations at a higher detailed level but also as a methodology to test the mechanical behaviour of new materials belonging to a random macro-structure subjected to certain boundary conditions.

Difficulties are encountered when testing the framework with a model that allows for softening and localisation. The choice of the boundary conditions (*displacement interface with linear interpolation*) makes it impossible for the model to predict a correct failure pattern. Strains cannot localise at the boundaries of the meso-structure and, for that reason, an artificial distribution of the strain and a more ductile global response is observed. At the same time the framework is not capable of simulating more complex localisation tests. It is not possible to propagate the localisation zone in an arbitrary direction inside the cell because of the strong constrain of the boundary interface. It can be concluded that the choice of a linear interpolation of the displacement boundary interface is not sufficient for our case of study.

An alternative can be the implementation of a force based interface. In this case the Lagrange multipliers need to be used to prescribe forces at the boundary and fullfill both equilibrium and compatibility between meso and macro structures. More research has to be carried out to study the possibility of adapting a force based interface into a strain driven multi-scale framework.

The formulation of a correct boundary interface is crucial for a realistic failure analysis in a multi-scale context.

Appendix A

Gradient enhanced damage model

In the present study the gradient enhanced damage model is chosen as a continuous approach to tackle failure processes at the meso level. The model provides regularisation and for this reason it is considered mesh independent. It is appropriate to simulate fracture processes in brittle materials (see Appendix B) reproducing realistic failure patterns of complex heterogeneous structures with a fair numerical and computational effort.

A brief mathematical formulation is provided in the following section.

A.1 Basics of continuum damage mechanics

Damage mechanics is a branch of continuum mechanics that incorporates changes in the micro-structural level via a finite number of scalar or tensor-valued internal variables (Lemaitre and Chaboche [16]). Damage is related to plasticity because the material history on the stress evolution is also incorporated in the continuum theory, although it differs from plasticity because in a damage context unloading does not occur elastically. This is caused by the degradation of the elastic stiffness matrix considered in the unloading branch. Generalizing to three dimensions and assuming that all damage effects can be reproduced by a single variable we can relate the stress tensor, σ, and strain tensor, ϵ, through

$$\boldsymbol{\sigma} = (1-\omega)\boldsymbol{D}^e\boldsymbol{\varepsilon}, \tag{A.1}$$

ω being an internal variable (damage parameter) which signifies how much of the system is damaged. $\omega = 0$ denotes a virgin material with no damage while $\omega = 1$ denotes a fully damaged material. $\boldsymbol{D}^e$ is the elastic stiffness matrix which can be expressed in terms of the Lamé constants or both Young's modulus E and the Poisson's ratio ν. Damage growth is controlled by the damage loading function

$$f(\tilde{\varepsilon}, k) = \tilde{\varepsilon} - k, \tag{A.2}$$

where k is a history dependent parameter which reflects the loading history and $\tilde{\varepsilon}$ an equivalent strain that is an invariant of the strain tensor. The history parameter goes from a initial value k_0 where the damage is supposed to start and grows memorizing the larger value of the $\tilde{\varepsilon}$. In the present study a Mazar's definition is considered for the $\tilde{\varepsilon}$ as a function of principal strains

$$\tilde{\varepsilon} = \sqrt{\sum_{i=1}^{3} (< \varepsilon_i >)^2}, \tag{A.3}$$

where $< \varepsilon_i >= \varepsilon_i$ if $\varepsilon_i > 0$ and $< \varepsilon_i >= 0$ otherwise. The history parameter k never decreases so its rate $\dot{k}$ is strictly positive. The structure of the loading function can, just as for plasticity, be formalized using the Kuhn-Tucker conditions

$$f \leq 0, \; \dot{k} \geq 0, \; f\dot{k} = 0. \tag{A.4}$$

Furthermore, an evolution law for the damage variable ω is defined as a function of the history parameter $\omega = \omega(k)$.

In our case an exponential softening damage evolution law is chosen. For this the following relation holds:

$$\omega = 1 - \frac{k_0}{k}[1 - \alpha + \alpha e^{-\beta(k - k_0)}], \tag{A.5}$$

where α and β are material parameters: β controls the slope of the softening branch (giving more negative slopes for larger values of β) and α sets the residual strength.

A.2 Gradient-enhanced damage formulation

The former formulation corresponds to a classical local damage model. It is well known that without a regularisation strategy strain localizes to a narrowing band of infinitesimal width. For this reason strains approach to infinity in this area and the problem becomes ill-posed.

A way to circumvent this drawback is the introduction of a non-local strain quantity (see [1]). In the present formulation the non-local equivalent strain is presented in an implicit differential format.

Considering $\tilde{\varepsilon}$ as state variable, this differential formulation can be expressed in the spirit of

$$\tilde{\varepsilon}(\boldsymbol{x}) = \tilde{\varepsilon}_{nl}(\boldsymbol{x}) - c\nabla^2 \tilde{\varepsilon}_{nl}(\boldsymbol{x}), \tag{A.6}$$

$\tilde{\varepsilon}_{nl}(\boldsymbol{x})$ being the non-local equivalent strain and $\tilde{\varepsilon}(\boldsymbol{x})$ the local equivalent strain. Moreover $c = \frac{l^2}{2}$ and l is the internal length scale of the gradient enhancement. This parameter means the internal length scale needed to regularise the localisation of deformation and is related to the width of the localisation band.

The natural boundary condition specified for the previous equation is

$$\boldsymbol{n}\nabla\tilde{\varepsilon}_{nl} = 0, \tag{A.7}$$

where n is the unit normal to the boundary.

The Governing equations are both equilibrium in the domain and the implicit gradient-enhancement

$$\begin{gathered} \nabla \cdot \boldsymbol{\sigma} + \boldsymbol{b} = \boldsymbol{0} \\ \tilde{\varepsilon}(\boldsymbol{x}) = \tilde{\varepsilon}_{nl}(\boldsymbol{x}) - c\nabla^2 \tilde{\varepsilon}_{nl}(\boldsymbol{x}). \end{gathered} \tag{A.8}$$

The Boundary Conditions are the ones defined on Γ_t (natural), Γ_u (essential) and the natural boundary conditions on $\partial\Omega$ for the non-local equivalent strain.
The Constitutive Relations specify (in this order) the stress/strain relation, the damage evolution law, the history variable definition, the equivalent strain definition, the loading function and the Kuhn-Tucker loading unloading conditions

$$\begin{gathered} \boldsymbol{\sigma} = (1 - \omega)\boldsymbol{D}^e \boldsymbol{\varepsilon} \\ \omega = \omega(k) \\ k = max(k; \tilde{\varepsilon}_{nl}(\tau), \tau \leq t) \\ \tilde{\varepsilon}_{nl} = \tilde{\varepsilon}_{nl}(\boldsymbol{\varepsilon}) \\ f(\tilde{\varepsilon}_{nl}) = \tilde{\varepsilon}_{nl} - k\tilde{\varepsilon}_{nl} \\ f \leq 0, \dot{k} \geq 0, f\dot{k} = 0, \end{gathered} \tag{A.9}$$

A detailed finite element implementation of the gradient enhanced damage is given in [24] and [21].

Appendix B

Representative volumes for elastic, hardening and softening materials

B.1 Modeling a three phase brittle material

The meso-structure of a brittle material such as concrete can be simulated using a three phase structure composed by a matrix, aggregates and a brittle interfacial transition zone (ITZ) around them [25] (Figure B.1).

With the use of a gradient damage model and a particular arrangement of material parameters realistic failure patterns can be simulated.

In this study, c is considered as a material parameter and for that, a similar width of the damage band is assumed for all samples. Particles are designed to behave stiffer than the matrix which is, at the same time, stiffer than the ITZ.

The value of k_0 is different for each material. In order to reproduce with accuracy what is observed in the reality, damage is imposed to begin in the ITZ. After that the matrix will enter in damage as well but the particles are not supposed to be damaged during the whole test. For this, the smallest value of k_0 is assigned to the ITZ, the matrix will have a larger k_0 and finally the particles will have such a large value of k_0 that damage

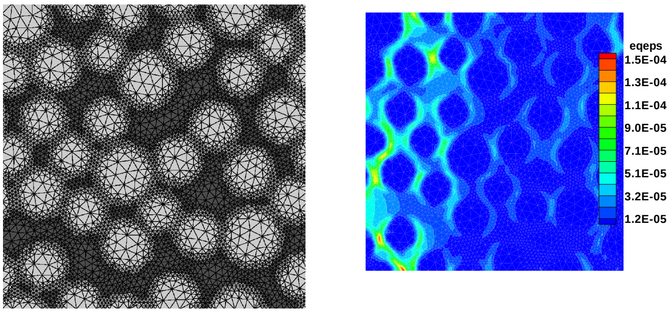

Figure B.1: Granular material with aggregates matrix and an interfacial transition zone (left). Equivalent strain contours for the tensile test (right).

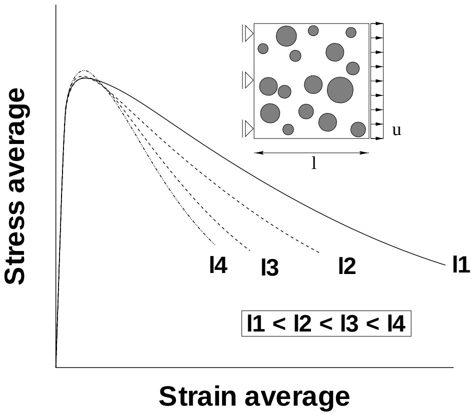

Figure B.2: Meso cell size effect in softening.

will not take place because the deformation rates reached during the test will be much smaller. Therefore, we can make sure that the particles will behave elastically during the whole deformation path.

An example of a failure pattern is given is Figure B.1 when the specimen is loaded in uniaxial horizontal tension.

B.2 RVE considerations and size dependency

According to Hashin [12] a definition of a Representative Volume Element (RVE) can be enunciated as follows:

The RVE is a model of the material to be used to determine the corresponding effective properties for the homogenised macroscopic model. The RVE should be large enough to contain sufficient information about the micro-structure in order to be representative, however it should be much smaller than the macroscopic body.

In [10] a statistical procedure is described to quantify the RVE size of a composite structure under certain loading conditions for the elastic, hardening and softening regimes.

It is concluded that the size of a representative RVE can be calculated with a relatively high accuracy for elastic and hardening materials. In the case of softening materials no RVE size can be found due to a phenomenological size effect. When increasing the size of the specimen the overall response turns to be much brittle (Figure B.2). The effect can be explained when considering the effect on the dissipated fracture energy of an increasing area that is experiencing unloading.

Bibliography

[1] Z.P. Bazant and G. Pijaudier-Cabot. Nonlocal continuum damage, localization instability and convergence. *Journal of Applied Mechanics*, 55:287–293, 1988.

[2] I. Doghri and A. Quaar. Homogenization of two-phase elasto-plastic composite materials and structures. study of tangent operators, cyclic plasticity and numerical algorithms. *International Journal of Solids and Structures*, 40:1681–1712, 2003.

[3] C.A. Felippa. Solution of equations with skyline-stored symmetric coefficient matrix. *Computers and structures*, 5:13–25, 1975.

[4] C.A. Felippa. *Introduction to Finite Element methods (Lecture notes)*. Department of Aerospce Engineering Sciences. University of Colorado, Boulder, Colorado (USA), 2003.

[5] C.A. Felippa and K.C. Park. The construction of free-free flexibility matrices for multilevel structural analysis. *Comp. Methods Appl. Mech. Engrg*, 191:2111–2140, 2002.

[6] F. Feyel. A multilevel finite element method (fe^2) to describe the response of highly non-linear structures using generalized continua. *Comp. Methods Appl. Mech. Engrg*, 192:3233–3244, 2003.

[7] M.G.D. Geers, V.G. Kouznetsova, and W.A.M. Brekelmans. Multi-scale first-order and second-order computational homogenization of microstructures towards continua. *Int. J. Multiscale Comput. Engrg.*, 1:371–386, 2003.

[8] I.M. Gitman. *Representative volumes and multi-scale modeling of quasi-brittle materials.* PhD thesis, Technische Universiteit Delft, 2006.

[9] I.M. Gitman, H. Askes, and L.J. Sluys. Multi-scale modelling of quasi-brittle material. *Euro-C 2006 - Computational Modelling of Concrete Structures, eds. G. Meschke, R. de Borst, H. Mang and N. Bicanic*, Mayrhofen (Tirol) Austria:97–107, 2006.

[10] I.M. Gitman, H. Askes, L.J. Sluys, and O. Lloberas. The concept of representative volume for elastic, hardening and softening materials. *Proceedings of XXXII*

International Summer School-Conference "Advance problems in Mechanics", Saint Petersburg (Repino) Russia:180–184, 2004.

[11] S. Gosh, K. Lee, and S. Moorthy. Two-scale analysis of heterogeneous elastic-plastic materials with asymptotic homogenization and voronoi cell finite element model. *Comp. Methods Appl. Mech. Engrg*, 132:63–116, 1996.

[12] Z. Hashin. Analysis of composite materials. *a survey ASME J. Appl. Mech.*, 50:481–505, 1983.

[13] A. Ibrahimbegović and D. Marcovič. Strong coupling methods in multi-phase and multi-scale modeling of inelastic behaviour of heterogeneous structures. *Comp. Methods Appl. Mech. Engrg*, 192:3089–3107, 2003.

[14] V. G. Kouznetsova. *Computational homogenization for the multi-scale analysis of multi-phase materials.* PhD thesis, Eindhoven University of Technology, Mechanical Engineering Department, December 2002.

[15] V.G. Kouznetsova, M.G.D. Geers, and W.A.M. Brekelmans. Multi-scale second-order computational homogenization of multi-phase materials: a nested finite element solution strategy. *Comp. Methods Appl. Mech. Engrg*, 193:5525–5550, 2004.

[16] J. Lemaitre and J.L. Chaboche. *Mechanics of solid materials.* Cambridge University Press, The Edimburg Building, Cambridge CB2 2RUm UK, 1990.

[17] O. Lloberas. *Representative volume for elastic, hardening and softening materials.* MsC thesis, Universitat Politècnica de Barcelona, Barcelona (Spain), 2004.

[18] D. Marcovič and A. Ibrahimbegović. On micro-macro interface conditions for micro scale based fem for inelastic behaviour of heterogeneous materials. *Comp. Methods Appl. Mech. Engrg*, 193:5503–5523, 2003.

[19] C. Miehe and A. Koch. Computational micro-to-macro transitions for discretized micro-structures undergoing small strain. *Archives in Applied Mechanics*, 72:300–317, 2002.

[20] S. Nemat-Nasser and M. Hori. *Micromechanics: overall properties of heterogeneous materials.* Elsevier, second ed. Amsterdam, 1999.

[21] R. Peerlings. *Enhanced damage modelling for fracture and fatigue.* PhD thesis, Eindhoven University of Technology, 1999.

[22] O. Pierard, C. Friebel, and I. Doghri. Mean-field homogenization of multi-phase thermo-elastic composites: a general framework and its validation. *Composites Science and Technology*, 64:1587–1603, 2004.

[23] J.S. Przemieniecki. *Theory of matrix structural analysis.* McGraw-Hill, USA, 1968.

[24] A. Simone. *Assessment of a Gradient-Enhanced Continuum Damage Model and its Imlementation.* TU Delft Report, Delft University of Technology, 2000.

[25] Martijn Stroeven, Harm Askes, and L. J. Sluys. A numerical approach to determine representative volumes for granular structures. *WCCMV, Fifth World Congress on Computational Mechanics, Eds: H.A. Mang, F.G. Rammerstorfer, J. Eberhardsteiner*, 2002.

[26] P.M. Suquet. *Plasticity today: modeling, methods and applications, chapter Local and global aspects in the mathematical theory of plasticity.* Elsevier Applied Science publishers, London, 1985.

[27] R.L. Taylor. *FEAP–A Finite Element Analysis Program.* Department of Civil and Environmental Engineering, Berkeley, California, 1999.

[28] E.L. Wilson. The static condensation algorithm. *International Journal for Numerical Methods in Engineering*, 8:198–203, 1974.

[29] O.C. Zienkiewicz and R.L. Taylor. *The Finite Element Method. Volume I: The basis.* (5th edition) Butterworth-Heinemann, Oxford, 2000.